ABSTRACT

LIGHT TRANSPORT AND AMPLIFICATION FOR A PROOF-OF-PRINCIPLE EXPERIMENT OF OPTICAL STOCHASTIC COOLING

M. B. Andorf, Ph.D.
Department of Physics
Northern Illinois University, 2018
Dr.Philippe Piot, Director

The Optical Stochastic Cooling (OSC) is a proposed technique that holds promise for the cooling of heavy-ions and dense TeV scale hadron beams. In the OSC a particle radiates a short wave-packet in an upstream "pickup" undulator and is made to interact with its own radiation in a downstream "kicker" undulator providing a corrective energy kick. In this thesis we present formulas and wave-optics simulations to compute the single-particle kick amplitude. The wave-optics simulations are further used to model amplification of the pickup radiation in a solid-state gain medium. This research was carried out in preparation of a proof-of-principle demonstration of the OSC in Fermilab's Integrable Optics Test Accelerator (IOTA) using 100 MeV electrons.

NORTHERN ILLINOIS UNIVERSITY
DE KALB, ILLINOIS

AUGUST 2018

LIGHT TRANSPORT AND AMPLIFICATION FOR A PROOF-OF-PRINCIPLE EXPERIMENT OF OPTICAL STOCHASTIC COOLING

BY

M. B. ANDORF

A DISSERTATION SUBMITTED TO THE GRADUATE SCHOOL
IN PARTIAL FULFILLMENT OF THE REQUIREMENTS
FOR THE DEGREE
DOCTOR OF PHILOSOPHY

DEPARTMENT OF PHYSICS

Dissertation Director:
Dr.Philippe Piot

ACKNOWLEDGEMENTS

First and foremost, I would like to thank my adviser Philippe Piot for giving me the opportunity to work on this exciting project, for the insightful feedback and advice and always being a source of encouragement in my developing as a physicist. Next, I want to thank Valeri Lebedev who functioned as an informal adviser during my time at Fermilab. I will always be grateful to have had the opportunity to work with and learn from a scientist with so clear a vision of our project as he.

I am grateful to Jinhao Ruan and Jonathan Jarvis with whom I collaborated much with on this project. Thank you to Swapan Chattopadhyay for the support and encouragement. I would also like to thank my thesis committee for their time and effort, Laurence Lurio, Mike Syphers and especially Alexander Zholents for his careful reading and thoughtful feedback of this thesis.

Lastly I thank my loving family without whose support none of this work would be possible.

This work was supported by the US Department of Energy under contract DE-SC0013761 to Northern Illinois University. Fermilab is managed by the Fermi Research Alliance, LLC for the U.S. Department of Energy Office of Science Contract number DE-AC02-07CH11359.

TABLE OF CONTENTS

Chapter Page

LIST OF TABLES

LIST OF FIGURES

Figure Page

LIST OF APPENDICES

CHAPTER 1

INTRODUCTION

Pariticle accelerators capable of colliding two counter-propagating beams are an essential tool for discoveries in elementary particle physics. Upon the collision exotic particles are generated whose rate of production, for a fixed beam energy, is determined the beam luminosity. A general figure-of-merit for an accelerator is the emittance or equivalently the volume in phase space occupied by the beam.

In an accelerator based light source reducing the beam emittance increases the brightness of the synchrotron radiation and consequently improves the quality of the data obtained by synchrotron light users over a variety of techniques such as X-ray diffraction. In these machines the emittance is optimized by designing the ring lattice to take full advantage of the damping effects of synchrotron radiation while carefully mitigating emittance growth stemming from the quantum nature of the emitted radiation.

In a hadron or heavy-ion collider small emittance is desired to increase the beam luminosity and lifetime. However owing to the increased mass of these particles radiative damping has a negligible effect on the emittance. Thus two methods of beam cooling[1], electron [1] [2] and stochastic cooling have been developed and successfully used in a variety of machines. For dense beams at TeV scale energies neither of these techniques are effective at cooling and so alternative methods of beam cooling are of considerable interest. Namely proof-of-principle experiments of the Coherent-electron-Cooling currently being pursued at Brookhaven National Laboratory [3] and the Optical Stochastic Cooling (OSC) [4, 5] at Fermilab [6] and

[1]The use of the word 'cooling' comes from the notion that in the moving frame of the beam, particles oscillate around a central point in much the same way as the molecules of a hot gas bounce around in a container.

also Cornell University. After a sucessful demonstration of the OSC the tecnique can be used to to help store high intensity beams [7], and cool different types of beam species [8, 9, 10].

1.1 Motivation for the OSC

The OSC is very similar to the stochastic cooling from which its name is derived. Stochastic cooling was invented in 1968 by Simon van der Meer [11, 12, 13] and was subsequently applied to the cooling of antiprotons at CERN resulting in the discovery of the Z and W bosons in 1983. Qualitatively, stochastic cooling consist in (i) detecting a signal providing information on a particle's displacement x, (ii) transporting and manipulating this signal and, (iii) coupling back the transported signal to the same particle downstream. The signal is detected via a 'pickup' while the coupling of the signal back onto the beam is performed via the 'kicker'. After one pass through the cooling system the displacement is modified as [14]

$$x_c = x - \lambda x. \tag{1.1}$$

where λ is the corrective-kick strength. From the latter equation we ideally want to set $\lambda = 1$ so that when the correction is applied the particles displacement is zero. However we must bear in mind that when we apply this corrective kick to our test particle we will also inadvertently detect and apply a kick from N_s other particles entering the cooling system within a time frame of $\pm T/2$ where $T \equiv 1/(2W)$ and W is the bandwidth of the cooling system. The collection of these N_s particles is often referred to as a 'sample-slice' of the beam. Introducing $g \equiv \lambda N_s$ the change in the particles displacement becomes

$$\Delta x = -\frac{g}{N_s} x - g\langle x \rangle_{s'} \tag{1.2}$$

where the first term constitutes the 'coherent' (correcting) kick while the second term is the 'incoherent' heating contribution from neighboring particles and the angled-brackets indicate an average. By treating the incoherent term as a randomly fluctuating variable the reduction of the rms displacement of the sample-slice is found to be

$$\Delta(x_{rms}^2) = -\frac{(2g - g^2)}{N_s} x_{rms}^2. \tag{1.3}$$

From the latter equation a minimum in the rms spread is achieved when $\frac{d\Delta(x_{rms}^2)}{dg} = 0$ yielding the optimal gain $g = 1$. Therefore considering the single particle model of Eq. 1.1 we have $x_c = x - x/N_s$ and so we can only correct (on average) a fraction x/N_s of the particle's displacement per pass under optimal conditions.

The pickup and kicker for stochastic cooling consist of either planar or three dimensional stripline electrodes. State-of-the art systems, such as those used in the Accumulator and Debuncher at Fermilab, reached an operating band of W=4-8 GHz [15]. So that $T \approx 120$ ps.

The motivation for the OSC is that by transitioning to optical frequencies W can be increased by approximately four orders of magnitude in effect significantly reducing T or equivalently N_s and consequently the damping time. This is done by replacing the microwave based pickup and kicker plates with undulators.

Qualitatively the OSC works in the following way: a particle radiates a short electromagnetic wave-packet in the pickup. Then the particle trajectory is separated from the optical wave using a 'chicane' beamline. The path length of this chicane will depend on the particles deviation with respect to some ideal reference particle. Meanwhile the wave-packet radiated in the pickup will go through an optical transport system consisting of lenses and possibly an optical amplifier. The path length through the chicane and the total optical delay of the transport line are tuned such that the reference particle will arrive at the entrance of the

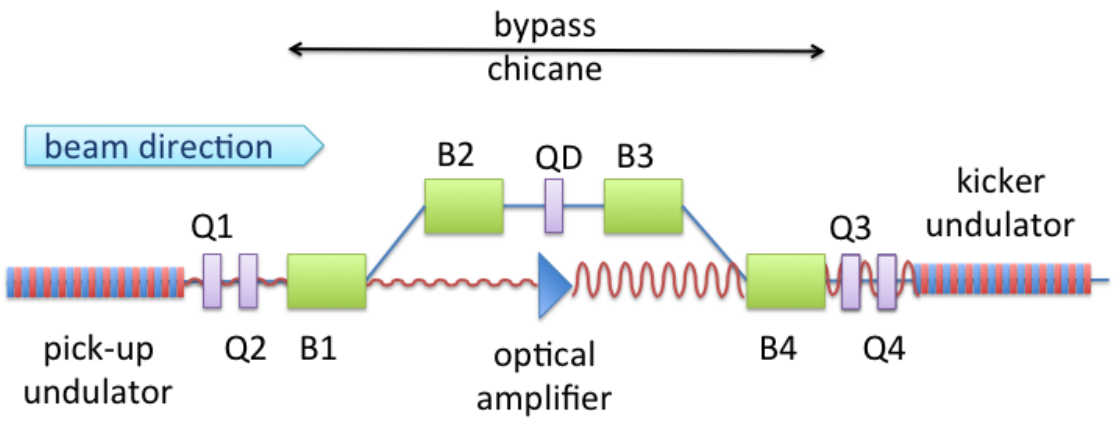

Figure 1.1: Schematic of the OSC. The labels "B" and "Q" respectively correspond to dipole and quadrupole electromagnets. The blue line indicates the particle path while the red wiggle trace corresponds to the optical signal.

kicker in phase with its own radiation from the pickup such that no net energy exchange occurs between the two. However an arbitrary particle is delayed or advanced according to its position with respect to the reference particle in the phase-space. Therefore it will experience a net energy exchange resulting in a corrective kick being applied on the particle when the delay is properly set. It should be noted that although the kick is in energy, when applied at a location in the ring with coupling between longitudinal and horizontal degrees of freedom, OSC can be used for horizontal damping.

The OSC test in IOTA will take place in two phases: a passive phase which uses only a focusing lens for the transport line; and an active phase utilizing an amplifier based on Cr:ZnSe. Although a passive demonstration is interesting from a physics perspective OSC for hadrons or heavy-ions requires an amplifier with 20-30dB of gain. The active test is then an important step to making OSC a viable beam cooling technique in a real collider.

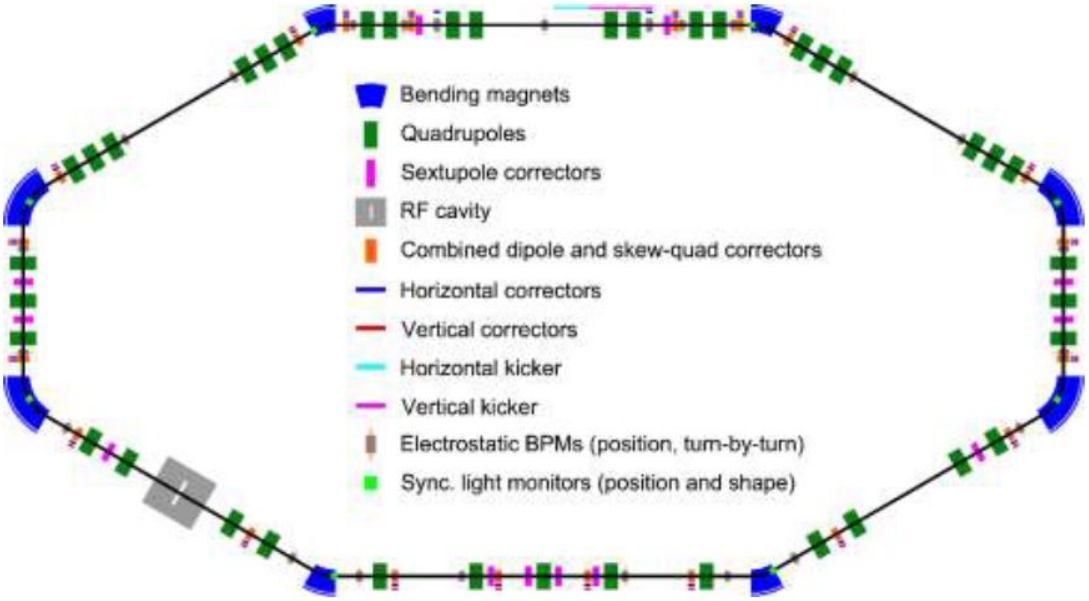

Figure 1.2: The layout of IOTA. OSC will occupy the bottom straight section (chicane and undulator magnets not shown).

1.2 The IOTA ring

The Integrable Optics Test Accelerator (IOTA) is currently under its final stages of construction at Fermilab [16]. The accelerator will have the capability of operating with either electrons with energies of up to 150 MeV or protons with momentum of 70 MeV/c. The motivation of its construction is the advancement of the 'Intensity-Frontier' in accelerators needed to support neutrino physics studies [17]. IOTA will provide an experimental test facility to address fundamental beam physics problems, such as space-charge compensation and halo formation, that emerge when accelerating and storing intense Mega-Watt class proton beams.

The ring is made up of 8 bends (four 30-deg and four 60-degree dipole magnets) and focusing is done with 39 quadrupole in 20 families. The layout is shown in Fig. 1.2 where injection

is done from the top, electrons circle clockwise and the OSC experiment will occupy the approximately 6 m bottom straight of the 40 m circumference ring.

1.3 Overview of this report

This dissertation explores the optical aspects of the OSC. Specifically, the work focuses on understanding the properties of undulator radiation emitted by a particle in the pickup, the propagation and manipulation of the associated optical signal to the kicker and its coupling back on the particle. The work especially developed a model of the optical transport that enabled the investigation of the proposed proof-of-principle experiment on the OSC in IOTA. The optical transport was modeled analytically along with an available wave-optics numerical framework adapted to our problem. Using realistic optical wave properties at the kicker location, the energy exchange between the field and particle was quantified including a variety of non-ideal conditions (e.g. chromatic aberrations) in the optical transport. Additionally, a single-pass optical amplifier was designed in support of the active phase of the OSC experiment at IOTA. Finally, a model of the OSC was implemented in ELEGANT to test the predicted amplitude dependent horizontal damping rates.

The dissertation is organized as follows. Chapter 2 covers the basic principles of the OSC from a heuristic account of the coupling between particle and electromagnetic wave in the kicker to the OSC's effects on singe-particle dynamics in the accelerator. In Chapter 3 a model of the pickup radiation and focusing is developed while in Chapter 4 a numeric wave-optics platform is used to confirm and expand our understanding of the OSC kick. In Chapter 5 a model of a single-pass amplifier is developed and used to design an amplifier for the active OSC test in IOTA. A diagnostic technique for timing the arrival of the pickup

radiation to the particle is discussed in Chapter 6 and finally in Chapter 7 horizontal cooling of the OSC in IOTA is simulated with ELEGANT.

CHAPTER 2

PRINCIPLES OF OPTICAL STOCHASTIC COOLING

2.1 OSC Basics

2.1.1 Particle Motion in an undulator

In this section we derive the trajectory for a particle passing through an undulator. These equations can then be used to compute the energy transfer between a particle and an electromagnetic traveling wave co-propagating through an undulator. The magnetic field of an undulator can be approximated as

$$\boldsymbol{B}(z) = \begin{cases} B_o \cos(k_p z)\hat{\boldsymbol{y}} & |z| \leq L_u/2 \\ 0 & |z| > L_u/2 \end{cases} \tag{2.1}$$

where B_o is the peak magnetic field, $k_p \equiv 2\pi/\lambda_u$ and λ_u[1] is the undulator period, L_u is the undulator length, z is the longitudinal direction, and y is vertical with the main effect of the undulator causing oscillations in the horizontal x direction. The equations of motion can be found from the Lorentz force which in the absence of an electric field is given by

[1] Later on λ_u will also refer to the longitudinal damping rate from the OSC. By the context in which it appears the meaning of λ_u should be clear.

$\boldsymbol{F} = q\boldsymbol{v} \times \boldsymbol{B} = \gamma m \dot{\boldsymbol{v}}$ and a $\dot{}$ above a variable is used to refer to differentiation with respect to time. This yields a set of coupled differential equations[18]

$$\ddot{x} = -\frac{qB_o}{\gamma m}\dot{z}\cos(\omega_u t) \tag{2.2}$$

$$\ddot{z} = \frac{qB_o}{\gamma m}\dot{x}\cos(\omega_u t), \tag{2.3}$$

where $\omega_u = ck_u$ is the undulator frequency. The maximum deflecting angle experienced by the particle with respect to the z axis is small implying $\dot{x} \ll \dot{z}$. With this in mind we can integrate Eq. 2.2 by approximating $\dot{z} \approx \beta c$ to get

$$\dot{x} = -c\frac{K}{\gamma}\sin(\omega_u t) \tag{2.4}$$

where $K \equiv \frac{qB_o}{k_p mc}$ is the undulator parameter. Next we note that since the magnetic field does not do any work on the particle the kinetic energy remains constant implying[2] $\beta^2 c^2 = \dot{x}^2 + \dot{z}^2$. Solving for z in this equation yields an updated expression for the longitudinal velocity

$$\dot{z} = \beta c\left(1 - \frac{K^2}{2\gamma^2}\sin^2(\omega_u t)\right) \tag{2.5}$$

where the approximation $\dot{x} \ll \dot{z}$ was again used to perform a Taylor expansion out of the square root. From Eq. 2.5 it is seen that the average longitudinal velocity of the particle passing through the undulator is $c\bar{\beta}$ with

$$\bar{\beta} = \beta(1 - \frac{K^2}{4\gamma^2}). \tag{2.6}$$

[2] Although the particle will loose energy by radiating this loss is negligible on its motion in the undulator. For example a 100 MeV electron in IOTA will emit in a single pass through either the pickup or kicker approximately 50 meV a ratio of $5\times^{-10}$.

$\dot{x}$ and $\dot{z}$ can now be integrated yielding the particles trajectory

$$x(t) = \frac{K}{\gamma k_p}\cos(\omega_u t) \tag{2.7}$$

$$z(t) = \bar{\beta}ct + \frac{K^2}{8\gamma^2 k_p}\sin(2\omega_u t). \tag{2.8}$$

As might be expected the motion is oscillatory with a period equal to that of the undulator period.

2.1.2 Coupling between a particle and electromagnetic wave in an undulator

We now consider a horizontally polarized e.m. wave co-propagating with the particle through the kicker. An energy exchange between the particle and radiation field can take place because of the transverse motion of the particle. Again since the energy exchange is small compared to the total energy we ignore the effect on the particles motion in the kicker so that Eq's 2.7 and 2.8 can be used. For most wavelengths since both the particle motion and field are oscillatory the energy transfer averages to zero. However for certain wavelengths and phase this transfer can be made so that there a net energy exchange occurs. To find the condition for this to happen let t_u be the amount of time it takes the particle to travel through one period of the undulator. From Eq. 2.8 $t_u = \lambda_u/\bar{\beta}c$. In this time the particle would have fallen back relative to the light wave a distance $\delta z = ct_p(1-\bar{\beta})$. In order for the transfer to be continuous this distance should be set equal to the light wavelength, $\delta z = \lambda_o$. So we find

$$\lambda_o = \lambda_u(\frac{1}{\bar{\beta}} - 1). \tag{2.9}$$

Next noting that $1/\beta \approx 1 + 1/2\gamma^2$ and $1/(1 - \frac{4K^2}{\gamma^2}) \approx 1 + 4K^2/\gamma^2$ to first order $1/\bar{\beta} \approx 1 + 4K^2/\gamma^2 + 1/2\gamma^2$. Plugging this into Eq. 2.9 yields

$$\lambda_o = \frac{\lambda_u}{2\gamma^2}\left(1 + 1/2K^2\right). \tag{2.10}$$

This expression, often derived through quite different means, also relates the emitted light wavelength in the forward direction to the undulator period. Thus for OSC the pickup and kicker undulators should have the same period. Furthermore the pulse emitted from the pickup will have a length $\approx N_u\lambda_o$ where N_u is the number of periods. Then since the particle slips behind the light wave 1 cycle for each undulator period, it follows that the pickup and kicker should also have the same number of periods.

As a heuristic approximation the electric field of the radiation wave packet can be written $\boldsymbol{E}(t, z) = E_x \cos(\omega_o t - k_o z + \psi_p)\hat{x}$ where ψ_p is determined by the arrival time of the particle with respect to the light at the entrance of the kicker. From Eq. 2.10 it follows that $\omega_u = \frac{\omega_o}{2\gamma^2}(1 + K^2/2)$. Then using Eq. 2.8 yields the electric field acting on the particle inside the kicker:

$$\boldsymbol{E}(t) = E_x \cos(\omega_u t + \kappa \sin(2\omega_u t) + \psi_p) \tag{2.11}$$

where $\kappa \equiv \frac{K^2}{4+2K^2}$. The rate of energy change of the particle is given by $\frac{d\mathcal{E}}{dt} = q\boldsymbol{v} \cdot \boldsymbol{E}$ resulting in a total energy exchange in the undulator

$$\Delta\mathcal{E}_p = \frac{ecKE_x}{\gamma}\int_0^{N_u 2\pi/\omega_u} \cos\left(\omega_u t - \kappa \sin(2\omega_u t) - \psi_p\right)\sin(\omega_u t)dt. \tag{2.12}$$

Changing the integration variable to $\xi = \omega_u t$ and using the following two integral identities

$$\begin{aligned} \int_0^{2\pi} \cos\big(\xi - \kappa \sin 2\xi\big) \sin\xi d\xi &= 0 \\ \int_0^{2\pi} \sin\big(\xi - \kappa \sin 2\xi\big) \sin\xi d\xi &= \pi\big(J_0(\xi) - J_1(\xi)\big) \end{aligned} \tag{2.13}$$

yields

$$\Delta\mathcal{E}_p = \frac{eKE_xL_u}{2\gamma} \sin(\psi_p) F_u(\kappa) \tag{2.14}$$

where $F_u(\kappa) \equiv J_1(\kappa) - J_0(\kappa)$. E_x depends on the parameters of the pickup and focusing optics. It will be studied in detail in Chapters 3 and 4.

For the case of small undulator parameter K and an optical system with an angular acceptance $\theta_m >> 1/\gamma$ it will later be shown that $\Delta\mathcal{E}_p(\psi_p = \pi/2) \approx \Delta\mathcal{E}_{tot}$, is the total radiative loss of electron passing through both undulators in the absence of OSC. Or when OSC is included energy loss is modulated as

$$\Delta\mathcal{E}_{loss} = \Delta\mathcal{E}_{tot}\big(1 + \sin(\psi_p)\big). \tag{2.15}$$

For cooling $\psi_p = k_l s$ where s is the longitudinal displacement of the particle, with respect to the reference particle, upon traveling from pickup to kicker centers. s depends on the particles phase-space coordinates (again with respect to the reference particle) in the pickup and the transfer elements of the bypass chicane. Thus the OSC insertion is altering the energy loss of the particle with respect to its deviation.

2.2 Cooling in the longitudinal phase space

In a synchrotron accelerator particles perform stable oscillations about the "reference" particle in the longitudinal phase space. Introducing the relative offset energy $\delta = \frac{U-U_s}{U_s} = \frac{u}{U_s}$ and phase $\theta = \phi - \phi_s$ where U and ϕ are the energy and phase (in the radio-frequency (RF) cavity) and the subscript s indicates a quantity associated with the reference particle. These oscillations are the result of an interplay between the energy dependent time-of-flight to go around the ring and the (time dependent) RF cavity restoring[3] energy to the particle lost in the emission of synchrotron radiation.

2.2.1 Linear motion and particle damping

The longitudinal equations of motion for a particle in a synchrotron with an OSC system are derived in Appendix A. For the case of small amplitude oscillations $\theta \ll 1$ the longitudinal dynamics can be described by a set of two coupled first-order differential equations:

$$\begin{aligned} \dot{\theta} &= h\omega_s \eta \frac{u}{U_s} \\ \dot{u} &= -\frac{\omega_s}{2\pi} qV \cos(\phi)\theta - \frac{\omega_s k_o M_{56} \Delta\mathcal{E}}{2\pi} \frac{u}{U_s} \end{aligned} \tag{2.16}$$

where $s = M_{56}u$. Here and from now on M_{nm} is used to denote the transfer matrix element from pickup to kicker center and $\Delta\mathcal{E}$ is the kick amplitude obtained by setting $\psi_p = \pi/2$ in

[3] Because the undulator wavelength must be fixed and is determined only by the undulator parameters and beam energy, we assume the beam energy is not being boosted and the RF is only restoring radiative losses.

Eq. 2.14. The two equations above can be combined to yield a single second-order differential equation

$$\ddot{u} + \frac{\omega_s}{2\pi}\left(k_o M_{56}\frac{\Delta\mathcal{E}}{U_s}\right)\dot{u} + \Omega^2 u = 0 \tag{2.17}$$

where $\Omega_s \equiv \omega_s\sqrt{\frac{h\eta\cos\phi_s}{2\pi}\frac{qV}{\gamma mc^2}}$ is the synchrotron frequency. Eq. 2.17 has the form of a damped harmonic oscillator and hence has the solution $u(t) = u_o\exp(-\lambda_u t)\cos(\Omega_s' t)$. Where

$$\lambda_u = \frac{k_o M_{56}}{2\tau_s}\frac{\Delta\mathcal{E}}{U_s} \qquad \Omega_s' = \sqrt{\Omega_s^2 - \lambda_u^2}. \tag{2.18}$$

Figure 2.1 shows damping of the energy oscillations as a function of time and its corresponding trajectory in phase space.

In an electron ring the energy oscillations are also significantly damped because the radiative energy loss per turn, U_γ, depends on the particles energy as, $U_\gamma(U) \approx U_\gamma(U_s) + \left(\frac{dU_\gamma}{du}\right)u$ [19]. This leads to an estimate of the radiative damping rate

$$\lambda_{damp} = \frac{1}{2}\left(\frac{dU_\gamma}{du}\right)\frac{\omega_s}{2\pi} \approx \frac{U_\gamma}{U_s}\frac{\omega_s}{2\pi}. \tag{2.19}$$

In the previous section we saw the OSC modulates the energy loss of the particle while passing through the insertion; but in the absence of a high gain amplifier this modulation is small compared to the total radiative loss.[4] How then can passive OSC effectively cool? If we compute the ratio

$$\frac{\lambda_u}{\lambda_{damp}} = 2\pi\left(\frac{\Delta\mathcal{E}}{U_\gamma}\right)\frac{M_{56}}{\lambda_o} \tag{2.20}$$

then, since λ_o is on the order of μm and M_{56} is on the order of mm, we see OSC is still effective even when $\Delta\mathcal{E}$ is a few orders of magnitude smaller than U_γ. This is because, despite the seemingly clear dependence of U_γ on the damping rate in Eq. 2.19, the original

[4] For example for the 2.2 μm gives $\Delta\mathcal{E}$=22 meV while the total radiative loss throughout the rest of the ring is approximately 14 eV.

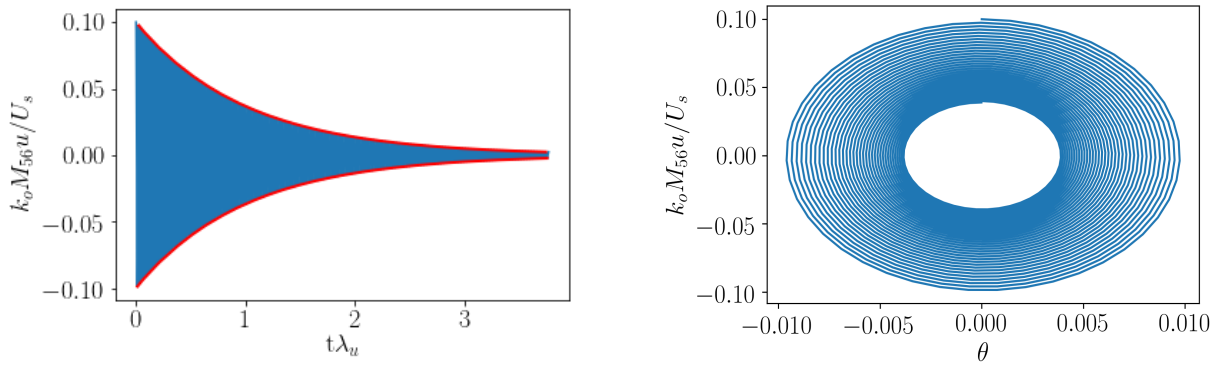

Figure 2.1: Left: $k_o M_{56} u(t)/U_s$ plotted over time (blue) with the envelope (red). Right: The particle trajectory in phase space.

source of the damping is $\frac{dU_\gamma}{du}$. Essentially for longitudinal damping the effect of the OSC is to increase $\frac{dU_\gamma}{du}$ by the amount $k_o M_{56} \frac{\Delta\mathcal{E}}{U_s}$.

2.2.2 Large amplitude motion and the OSC cooling range

In the previous section we assumed the argument in $\sin(k_o M_{56} u/U_s)$ was small enough to be expand the sin function to first order with a Taylor series. We now consider how the damping rate is modified according to the particles amplitude [20]. Let us define $a_u \equiv k_o M_{56} u_{max}/U_s$ where u_{max} is the maximum energy deviation the particle reaches over the course of one synchrotron oscillation. Then the relative kick is

$$\frac{\delta u}{U_s} = \frac{\Delta\mathcal{E}}{U_s} \sin\left(a_u \sin(\psi_u)\right) \tag{2.21}$$

where ψ_u is the particles synchrotron phase.

We see that for large enough values of a_u not only does the kick become nonlinear but the particle will begin to be kicked in the wrong direction for a portion of the synchrotron

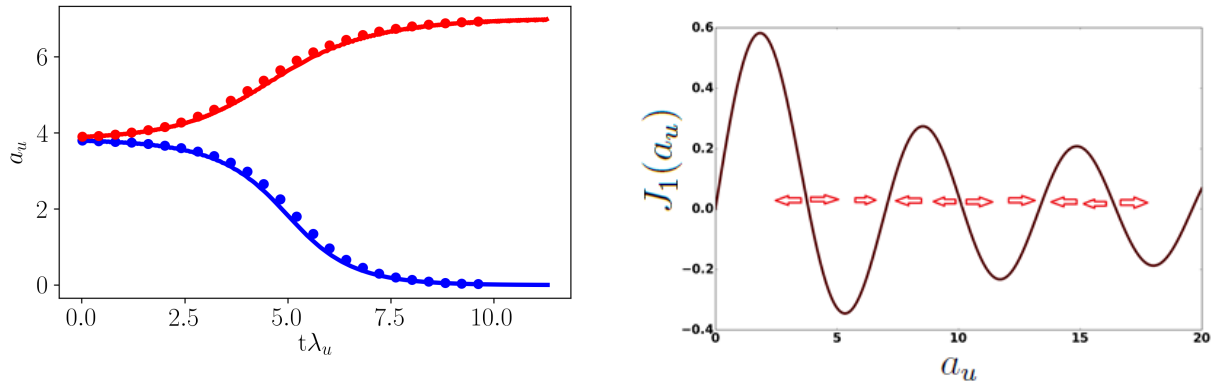

Figure 2.2: Left: (circles) $a_u(t)$ obtained by numerical integration of the equations of motion in the longitudinal phase space and extracting the envelope from their oscillatory solutions. (solid line) a_u is obtained directly by numerical integration of Eq. 2.23. Right: $J_1(a_u)$ is plotted arrows indicate whether a particle is being damped or excited

period which will significantly reduce its effective damping rate. At still larger values of a_u the average kick switches signs and the particle becomes anti-damped and consequently rejected from the cooled core of the beam. To find this boundary we average the cooling force over the synchrotron period and assume $\lambda_u \ll \Omega_u$ so that a_u does not change appreciably over one period. This yields the amplitude dependent damping rate

$$\lambda_u(a_u) = \frac{2\lambda_u}{a_u}\int_0^{2\pi} \sin\left(a_u \sin(\psi_u)\right)\sin(\psi_u)\frac{d\psi_u}{2\pi} = 2\lambda_u\frac{J_1(a_u)}{a_u} \tag{2.22}$$

where $J_1(x)$ is a Bessel function of the first kind. From the above it follows that the derivative of a_u is

$$\frac{da_u}{dt} = -2J_1(a_u)\lambda_u. \tag{2.23}$$

For cooling we need $J_1(a_u) > 0$ implying $a_u < \mu_{1,1} \approx 3.83$ where $\mu_{1,1}$[5] is the second zero of J_1. Notice that for small arguments $J_1(a_u) \approx a_u/2$ and so the above equation returns

[5]For naming zeros of the Bessel functions we use the following convention. $\mu_{n,j}$ is the jth zero for $J_n(x)$ where $j \geq 0$ and we count zeros at the origin

exponential damping at the rate λ_u as expected. Particles with amplitudes greater than $\mu_{1,1}$ are excited to the next zero of J_1 $\mu_{1,2} \approx 7.01$.

The left pane of Figure 2.2 shows a_u obtained through two different ways. The first is by numerically integrating the equations of motion in the longitudinal plane for particles with arbitrary amplitudes as obtained in Appendix A. These solutions will be oscillatory in nature. However we can interpret the positive valued envelope (which varies slowly compared to the synchrotron frequency) as being $a_u(t)$. Or more directly $a_u(t)$ can be found by numerical integration of Eq.2.23. We see good agreement with both approaches. As can be seen in the figure a bifurcation occurs at $a_u \approx 3.83$, amplitudes below this value are damped to zero while amplitudes above it are attracted to the next stable point $\mu_{1,2}$. We also see that particles with larger amplitudes take several damping periods, $1/\lambda_u$ to reach an equilibrium amplitude. The right pane of Figure 2.2 plots $J_1(a_u)$ with arrows indicating where a particle with an initial value of a_u will be attracted.

2.3 Cooling in longitudinal and horizontal degrees of freedom

The OSC can also be used to damp the particles betatron oscillations. As we already saw the corrective kick is only in the longitudinal direction and consequently in order to have horizontal cooling some coupling between the longitudinal and horizontal degrees of freedom need to be introduced. This is accomplished be designing the ring lattice to have non-zero dispersion in the OSC straight. Introducing D and $D' = \frac{dD}{dl}$ as the dispersion function

and its derivative the position of the particle can be written as $x(l) = x_\beta(l) + D(l)\frac{u}{U_s}$ and $x'(l) = x'_\beta(l) + D'(l)\frac{u}{U_s}$ where

$$\begin{aligned} x_\beta(l) &= \sqrt{\epsilon\beta(l)}\cos(\psi_x(l)) \\ x'_\beta(l) &= -\sqrt{\frac{\epsilon}{\beta(l)}}\Big(\sin(\psi_x(l)) + \alpha(l)\cos(\psi_x(l))\Big) \end{aligned} \tag{2.24}$$

and β, α are two of the three Twiss parameters[6]. ϵ is the particles Courant-Snyder invariant,

$$\epsilon = \beta(l)x'^2_\beta + 2\alpha(l)x_\beta x'_\beta + \gamma(l)x^2 \tag{2.25}$$

which in the absence of synchrotron radiation is conserved for particles experiencing forces linear in x. We have been using l to denote the independent variable for position around the ring however to avoid clutter in the notation we will stop explicitly showing the dependence. Accounting dispersion the particles longitudinal displacement becomes

$$s = M_{51}x_\beta + M_{52}x'_\beta + M_{56}\frac{u}{U_s} \tag{2.26}$$

and hence the longitudinal amplitude and cooling rates (Eq. 2.18) are modified as

$$a_u = ks_u\frac{u_{max}}{U_s} = k(M_{51}D + M_{52}D' + M_{56})\frac{u_{max}}{U_s} \tag{2.27}$$

and

$$\lambda_u = \frac{s_u}{2\tau_s}\frac{\Delta\mathcal{E}}{U_s}. \tag{2.28}$$

To find the horizontal damping rate we will again assume small amplitudes so that $k_o s \ll 1$. The damping from the OSC is again very similar in effect to synchrotron damping which

[6]The 3rd Twiss parameter is denoted by γ and all three are related by the relation $\beta\gamma - \alpha^2 = 1$. The parameters β and γ are not related to the relativistic factors β and γ used earlier in this chapter

can be used as a guide in calculating [19]. During the OSC energy kick a photon is absorbed or emitted in the direction of the particles transverse motion and hence the change in its position Δx and angle $\Delta x'$ is zero. Since the energy of the particle did clearly change we conclude there was a corresponding change to x_β and x'_β

$$\begin{aligned} \Delta x_\beta &= -\frac{\Delta \mathcal{E}}{U_s} D M_{51} x \\ \Delta x'_\beta &= -\frac{\Delta \mathcal{E}}{U_s} D' M_{52} x'. \end{aligned} \tag{2.29}$$

Like longitudinal damping, horizontal damping happens much more slowly than the period of betatron oscillations and so we will approximate the above changes as infinitesimal. Then the differential of ϵ is given by

$$d\epsilon = 2\beta x dx' + 2\alpha(x dx' + x' dx) + 2\gamma x' dx. \tag{2.30}$$

Inserting Eq's 2.24 and 2.29 into Eq. 2.30 and averaging over betatron oscillations yields

$$d\epsilon = -k_o \frac{\Delta \mathcal{E}}{U_s} \big(M_{51} D + M_{52} D' \big) \epsilon \tag{2.31}$$

where over the course of averaging we used

$$\langle x^2 \rangle = \epsilon\beta/2 \qquad \langle x x' \rangle = -\epsilon\alpha/2 \qquad \langle x'^2 \rangle = \epsilon\gamma/2. \tag{2.32}$$

By dividing both sides of Eq. 2.31 by τ_s to approximate the derivative we get

$$\frac{d\epsilon}{dt} = -k_o \frac{\Delta \mathcal{E}}{U_s \tau_s} \big(M_{51} D + M_{52} D' \big) \epsilon \tag{2.33}$$

the rate of change of the Courant-Snyder parameter. The above equation has the solution $\epsilon(t) = \epsilon_o \exp(2\lambda_x t)$ where

$$\lambda_x = -k_o \frac{M_{51}D + M_{52}D'}{2\tau_s} \frac{\Delta\mathcal{E}}{U_s} \tag{2.34}$$

is the damping rate (in amplitude) in the horizontal plane.

Using Eq. 2.28 we find

$$\lambda_u + \lambda_x = \frac{k_o M_{56}}{2\tau_s} \frac{\Delta\mathcal{E}}{U_s} \tag{2.35}$$

which matches Eq. 2.18 the longitudinal damping rate for when $\lambda_x = 0$. Dividing the above equation by λ_u and rearranging gives the cooling rates ratio

$$\frac{\lambda_x}{\lambda_u} = \frac{M_{56}}{M_{56} + DM_{51} + D'M_{52}} - 1 \tag{2.36}$$

confirming that dispersion is merely redistributing the total damping decrement between horizontal and longitudinal planes. Ultimately the total cooling is determined by M_{56} and partioned by dispersion and the relative values of M_{51}, M_{52} and M_{56} [21].

As in the case of 1-D cooling we want to consider what happens to particles with large amplitudes. The longitudinal displacement due to the transverse coordinates in the pickup is given by $M_{51}x_\beta + M_{52}x'_\beta$. Then averaging over betatron oscillations yields

$$a_x = k_o\sqrt{\epsilon s_x} = k_o\sqrt{\epsilon(\beta M_{51}^2 - 2\alpha M_{51}M_{52} + \gamma M_{52}^2)} \tag{2.37}$$

To find the damping rate of a single particle, now as a function of the particle's displacement due to both betatron and synchrotron motion we average the cooling force over both types of oscillations. Additionally we want to account for an error in the timing of the arrival

of the radiation wave-packet and reference particle resulting in the reference particle being given a kick $\delta u/U_s = \frac{\Delta\mathcal{E}}{U_s}\sin(\psi_{te})$. Doing this yields [21]

$$\begin{aligned}\begin{bmatrix}\lambda_x(a_x,a_u)/\lambda_x\\ \lambda_u(a_x,a_u)_u/\lambda_u\end{bmatrix} = &\\ &\begin{bmatrix}2/a_x\\ 2/a_u\end{bmatrix}\int_0^{2\pi}\int_0^{2\pi}\sin\Big(a_x\sin(\psi_x)+a_u\sin(\psi_u)+\psi_{te}\Big)\begin{bmatrix}\sin(\psi_x)\\ \sin(\psi_u)\end{bmatrix}\frac{d\psi_x}{2\pi}\frac{d\psi_u}{2\pi}\\ &= 2\begin{bmatrix}J_0(a_u)J_1(a_x)/a_x\\ J_0(a_x)J_1(a_u)/a_u\end{bmatrix}\cos(\psi_{te}).\end{aligned} \tag{2.38}$$

From the latter equation we can write a coupled set of first-order nonlinear differential equations

$$\begin{aligned}\frac{da_x}{dt} &= -2J_0(a_u)J_1(a_x)\cos(\psi_{te})\lambda_x\\ \frac{da_u}{dt} &= -2J_0(a_x)J_1(a_u)\cos(\psi_{te})\lambda_u\end{aligned} \tag{2.39}$$

which describes the particles trajectory in the (a_u, a_x) space.

We now consider how the cooling boundary is modified for the case of 2-D cooling. We can see immediately that when $\cos(\psi_{te}) > 0$ a timing error results only in a reduction in the cooling rates but leaves the cooling boundary unaffected. It is also clearly seen that fixed points occur only when both $J_0(a_u) = J_0(a_x) = 0$ or when $J_1(a_u) = J_1(a_x) = 0$. In Appendix B it is shown that J_0 fixed points correspond to saddle-points while J_1 fixed points are either stable/unstable nodes. Accounting that a_u and a_x are positive valued functions, then in addition to the origin there are three fixed points $A = (0, \mu_{1,1})$, $B = (\mu_{0,1}, \mu_{0,1})$ and $C = (\mu_{1,1}, 0)$ that sketch out the cooling boundary as shown in Fig. 2.3. The points A and C are J_1-type unstable nodes while the origin is stable. The point B is a saddle point. Particles inside the region sketched out by these points are damped while particles outside

are excited to another stable fixed point at a larger amplitude. The upper plot in Fig. 2.3 shows a phase portrait with sample trajectories in the (a_x, a_u) space assuming $\cos(\psi_{te}) > 0$. For a timing error greater than $\pm 1/2(\lambda_l/c)$ [mod2π], $\cos(\psi_{te}) < 0$ and saddle points remain in the same location but the stable and unstable nodes swap positions. This implies particles inside the cooling boundary are attracted to the points A and C. The phase portrait and sample trajectories are appear in the lower plot in Fig. 2.3.

2.4 Linear beam optics and the cooling range

Inside the boundary $a_x,\ a_u \leq \mu_{0,1}$ particles are damped simultaneously in both degrees of freedom. We define the cooling ranges as

$$\eta_{\sigma_u} = \frac{u_{max}}{\sigma_u} \qquad \eta_{\sigma_x} = \sqrt{\frac{\epsilon_{max}}{\epsilon_o}} \tag{2.40}$$

such that a particle with both $\epsilon < \epsilon_{max}$ and $u < u_{max}$ is inside this boundary.
In the linear optics approximation the cooling chicane consist of 4-dipoles and a defocussing quadrupole. Using a thin lens formulation with bend magnets having zero length and cooling rates equal in both planes the cooling ranges are given by [21]

$$\begin{aligned} \eta_{\sigma_u} &\approx \frac{\mu_{0,1}}{k_o \sigma_u \Delta s} \\ \eta_{\sigma_x} &\approx \frac{\mu_{0,1}}{2k_o \Delta s}\sqrt{\frac{D^{*2}}{\epsilon_o \beta^*}} = \frac{\mu_{0,1}}{2k_o \Delta s}\sqrt{\frac{A^*}{\epsilon_o}} \end{aligned} \tag{2.41}$$

where $\Delta s \approx M_{56}/2$ is the optical delay of the chicane and * denotes value at the chicane center. In the latter equation A^* is the dispersion invariant in the horizontal plane defined as

$$A = \beta D^2 + 2\alpha D D' + \gamma D'^2 \tag{2.42}$$

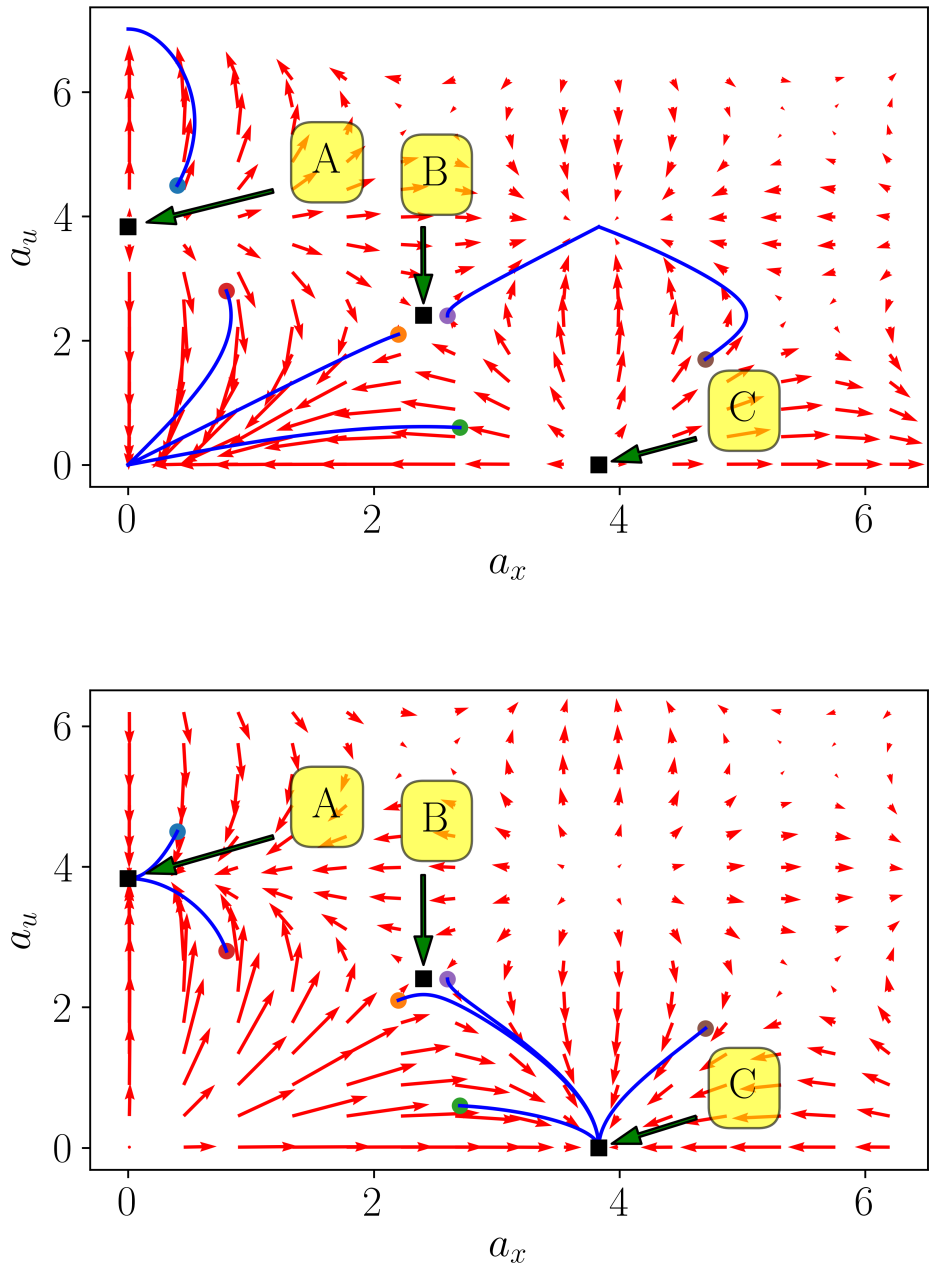

Figure 2.3: The phase portrait for particles in an OSC system with various example trajectories. Top pane is for the case that $\cos(\psi_{te}) > 0$ resulting in cooling of the particles within the cooling boundary. In the bottom pane $\cos\psi_{te} < 0$ resulting in particles being expelled from the cooling boundary to a new attractor.

which in the chicane center reduces to $A^* = D^{*2}/\beta$ on the account that the mirror-symmetry of the lattice functions about the chicane center implies $\alpha = D' = 0$ (see also section 7.2). Although a_x, $a_u \leq \mu_{0,1}$ ensures particle damping, as we already saw in Fig. 2.3 a particle can be cooled in one plane and heated in the other until it moves into this square cooling region and is subsequently damped in both planes. Therefore the expressions obtained in Eq. 2.41 should be considered useful estimates. In order to have sufficiently large cooling ranges in IOTA Δs was set to 2 mm and the undulator zero-angle wavelength to 2.2 μm. The notion of a cooling range leads to considerable constraints on the design of the amplifier as will be discussed in Chapter 5. Table 2.1 summarizes the chicane and beam parameters for the 2.2

Parameter	Value	Unit
ϵ_o	2.67	nm
σ_u	1.08×10^{-4}	-
η_{ϵ_o}	8.7	-
η_{σ_u}	4.6	-
β^*	0.13	m
D^*	0.48	m
s_x	3.5	μm
s_u	1.7	mm
M_{56}	3.8	mm

Table 2.1: Chicane and beam parameters for 2.2 μm OSC in IOTA.

μ OSC test in IOTA where values where obtained or computed from ELEGANT.

CHAPTER 3

ENERGY EXCHANGE THE PICKUP RADIATION AND PARTICLE IN THE KICKER

In the previous chapter we were interested in the particle dynamics of the OSC over many turns in the accelerator. We now wish to narrow the field of view and consider in detail the interaction (treated classically) between a single particle in the kicker and its own radiation that was emitted in the pickup during a single pass of the OSC insertion in order to compute $\Delta\mathcal{E}$. This analysis is useful in determining the undulator parameters and required optical system. We proceed by first expounding a general approach to computing the kick amplitude [21]. Then consider the case when $K \ll 1$ which will allow us to find relatively simple expressions for the electric field in the kicker and kick amplitude before then considering how these formulas are modified for the case of arbitrary (large) K. Finally we will consider aberrations in the optical transport line.

3.1 Electric field in the kicker center

To compute the kick amplitude we need to know the value of $E_x(x, z)$. As a first step towards this we consider a situation where the distance between the undulator centers, $2R_o$, is much larger than the pickup and kicker lengths L_u. Refocusing of the pickup radiation is achieved by symmetrically placing a single lens with a focal length $R_o/2$ between pickup and kicker centers. In this case the depth of field due to the finite length of the undulators can be neglected.

The electric field on the lens surface is computed from the Lienard-Wiechert formula (in the far zone)[1]

$$\boldsymbol{E}(r,t) = \frac{e}{c^2}\frac{\big(\boldsymbol{R}-\boldsymbol{\beta}R\big)\big(\boldsymbol{a}\cdot\boldsymbol{R}\big)-\boldsymbol{a}R\big(R-(\boldsymbol{\beta}\cdot\boldsymbol{R})\big)}{\big(R-(\boldsymbol{\beta}\cdot\boldsymbol{R})\big)^3}, \tag{3.1}$$

where $\boldsymbol{R} \equiv \boldsymbol{r}-\boldsymbol{r'} = R_o(\cos(\phi)\sin(\theta),\sin(\theta)\sin(\phi),\cos(\theta))$ is a vector from the point of emitted radiation $\boldsymbol{r'}$ to the observation point $\boldsymbol{r}$ on the lens surface and $\boldsymbol{a}$ is the acceleration. All values are taken at the emitter (retarded) time $t' = t - R_o/c$.

Recasting in a slightly different form the expressions for the velocity of an electron passing through an undulator in Eq. 2.4 and 2.5

$$v_x = -c\theta_e\sin(\omega_u t') \qquad v_z = c\left(1-\frac{1}{2\gamma^2}-\frac{\theta_e^2}{2}\sin^2(\omega_u t')\right) \tag{3.2}$$

where $\theta_e \equiv K/\gamma$ is the maximum angle of deflection of the particle, we can differentiate the above expressions with respect to time to find the acceleration allowing for the evaluation of the electric field on the lens surface:

$$E_x(r,t) = 4e\omega_u\gamma^4\cos(t'\omega_u)\times\frac{1+\gamma^2\big(\theta^2(1-2\cos^2(\phi)-2\theta\theta_e\sin(t'\omega_u)\cos(\phi)-\theta_e^2\sin(t'\omega_u)\big)}{cR_o\left(1+\gamma^2\big(\theta^2+2\theta\theta_e\sin(t'\omega_u)\cos(\phi)+\theta_e^2\sin^2(t'\omega_u)\big)\right)} \tag{3.3}$$

where the small angle approximations $\sin(\theta)\approx\theta$ and $\cos(\theta)\approx 1-\theta^2/2$ were used.

We next expand the field into a Fourier series

$$E_x = \sum_{n=0}^{\infty} E_{n\omega}(r,\theta)e^{in\omega(\theta)t} \tag{3.4}$$

[1]Unless otherwise noted formulas in this chapter use Gaussian units

and noting that only the fundamental will act resonantly[2] in the kicker we keep only the $n = 1$ harmonic

$$E_\omega(\boldsymbol{r}) = \frac{\omega(\theta)}{\pi} \int_0^{2\pi/\omega(\theta)} E_x(r,t) e^{-i\omega(\theta)t} dt. \tag{3.5}$$

with

$$\omega(\theta) = \frac{2\gamma^2 \omega_u}{1 + \gamma^2\left(\theta^2 + \theta_e^2/2\right)}. \tag{3.6}$$

Finally a modified Kirchoff formula is used to compute the focused undulator radiation in the kicker center

$$E(\boldsymbol{r}'') = \frac{1}{2\pi i c} \int_\Sigma \frac{\omega(\theta) E_\omega(\boldsymbol{r})}{|\boldsymbol{r} - \boldsymbol{r}''|} e^{i\omega(\theta)|\boldsymbol{r}-\boldsymbol{r}''|/c} d\Sigma \tag{3.7}$$

Σ is the surface of the lens where the vector $\boldsymbol{r}$ is located and $\boldsymbol{r}''$ is the coordinate of observation in the kicker. In the absence of dispersion in the lens a ray leaving the pickup with an angle θ will have a path lengthening equal to $2(R_o\theta^2/2)$ which is exactly compensated by a decrease in the glass thickness such that all rays take the same amount of time to travel from pickup to kicker centers[3]. This implies that the argument in the exponential of Eq. 3.7 reduces to a complex constant and can be dropped.

By integrating v_z in Eq. 3.2 with respect to time one obtains an expression for $R(t')$ which can be rearranged to give the observer time as a function of the emitter time

$$t(t') = \frac{t'}{2\gamma^2}\left(1 + \gamma^2\left(\theta^2 + \frac{\theta_e^2}{2}\right)\right) - \frac{\theta_e^2}{8\omega_u}\sin(2\omega_u t') - \frac{\theta\theta_e}{\omega_u}\cos(\phi)\cos(\omega_u t') \tag{3.8}$$

where the constant term R_o/c was dropped. Computing the derivative dt/dt' and using Eq. 3.3 and 3.8 enables integration of Eq. 3.5. Such a calculation is performed in the next section.

[2] See section. 4.3

[3] Taking into account that the depth of field is suppressed it also means that all rays have the same delay from travel between radiating and receiving points in the course of particle motion in the undulators.

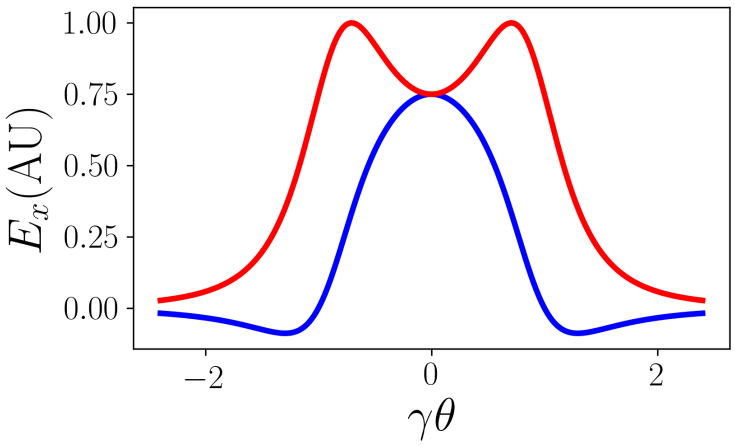

Figure 3.1: Normalized electric field amplitude at the lens surface for horizontal (blue) and vertical (red) planes.

3.1.1 OSC kick for small K

For the case when $K \ll 1$ the above equations simplify greatly and an analytic expression for E_x in the kicker center may be found. Eq. 3.3 becomes:

$$E_x = \cos(\omega_u t') \frac{4e\gamma^4 \omega_u \theta_e}{cR_o} \frac{1 + (\gamma\theta)^2(1 - \cos^2(\phi))}{\left(1 + (\gamma\theta)^2\right)^3} \tag{3.9}$$

and is plotted in Fig. 3.1. Additionally the expressions for $t(t')$ and $\omega(\theta)$ simplify to

$$t(t') \approx t'(1 + (\gamma\theta)^2)/2\gamma^2 \qquad \omega(\theta) \approx 2\gamma^2\omega_u/(1 + (\gamma\theta)^2). \tag{3.10}$$

Thus Eq. 3.5 can be rewritten as

$$E_\omega(r, \theta) = \frac{4e\gamma^4\omega_u^2\theta_e}{cR_o\pi} \frac{1 + (\gamma\theta)^2(1 - \cos^2(\phi))}{\left(1 + (\gamma\theta)^2\right)^3} \int_0^{2\pi/\omega(\theta)} \cos(\omega_u t') e^{-i\omega_u t'} dt' \tag{3.11}$$

making evaluation of the integral straight forward. Next plugging the obtained expression into Eq. 3.7, noting that $|\boldsymbol{r} - \boldsymbol{r}''| \approx R_o$ and assuming a circular lens aperture so that $d\Sigma \approx R_o^2 \theta d\theta d\phi$ gives

$$E_x = \frac{8e\gamma^6\omega_u\theta_e}{c^2}\int_0^{\theta_m}\int_0^{2\pi}\frac{1+(\gamma\theta)^2\left(1-2\cos^2\phi\right)}{\left(1+(\gamma\theta)^2\right)^4}\theta d\theta d\phi \tag{3.12}$$

we finally arrive at an expression for the electric field in the kicker center

$$E_x = \frac{4e\gamma^3\omega_u^2 K}{3c^2} f_L(\gamma\theta_m) \tag{3.13}$$

where $f_L(x) = 1 - 1/(1+x^2)^3$ and θ_m is the angle subtended by the lens and in order to evaluate the integral over θ we used

$$\int_0^{\theta_m}\frac{\theta d\theta}{\left(1+(\gamma\theta)^2)\right)^4} = \frac{1}{6\gamma^2}\left(1-\frac{1}{\left(1+(\gamma\theta_m)^2\right)^3}\right). \tag{3.14}$$

Since the depth of field has been suppressed by the large distance between the undulators and lens the amplitude of the electric field becomes constant over the length of the kicker. Then referring back to Eq. 2.14 we obtain the energy kick amplitude experienced by a particle: [4]

$$\Delta\mathcal{E} = \frac{2}{3}(e\gamma K k_u)^2 L_u f_L(\gamma\theta_m). \tag{3.15}$$

In the above expression for $\gamma\theta_m \ll 1$, $f_l(\gamma\theta_m) \approx 1$ and so, as discussed in chapter 2, the kick amplitude is equal to the total radiative energy loss of the particle passing through the pickup and kicker.

Figure 3.2 shows the relative kick strength as a function of angular acceptance of the

[4]Note that for $K \ll 1$ $F_u(\kappa) \approx 1$

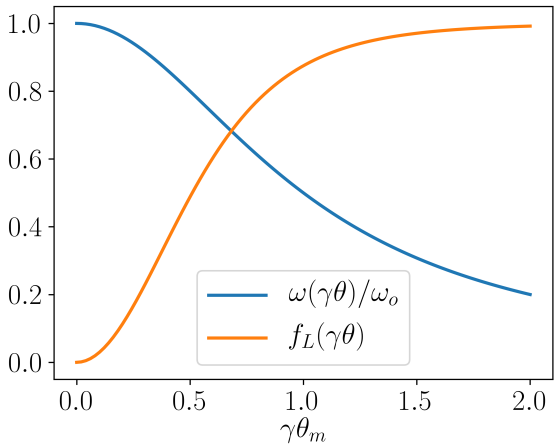

Figure 3.2: The relative cooling rate as dependent on the angular acceptance of the focusing lens (orange) and ratio of central to outermost angular frequency of the beam (blue)

focusing lens. We see that an acceptance of $\gamma\theta_m = 0.8$ results in approximately 80% of the theoretical maximum kick. This corresponds to a relative bandwidth $\Delta\omega/\omega_o$ of 40 %. This definition of the bandwidth is independent of the number of undulator periods. To obtain the actual bandwidth one has to account a finite number of undulator periods typically approximated as $\Delta\omega/\omega_o \approx 1/N_u$. For sufficiently large number of periods this additional spectrum widening can be neglected.

To find the transverse electric field distribution in the plane orthogonal to the axis and coming through the focal point the exponential in Eq. 3.7 accounting the phase advance correction must be restored. Let the observation point be $\boldsymbol{P''} = (R_o, \theta'', \phi'')$ then the distance off axis in the plane of the focal point is $\rho'' = R_o\theta''$ and Eq. 3.7 becomes

$$E_x(\rho'', \phi'') = \frac{8e\gamma^6\omega_u^2\theta_e}{c^2}\int_0^{2\pi}\frac{d\phi}{2\pi}\times \\ \int_0^{\theta_m}\frac{1+(\gamma\theta)^2(1-2\cos^2\phi)}{\left(1+(\gamma\theta)^2\right)^4}\exp\left(\frac{i\rho' k_o\theta\cos(\phi''-\phi)}{1+(\gamma\theta)^2}\right)\theta d\theta \tag{3.16}$$

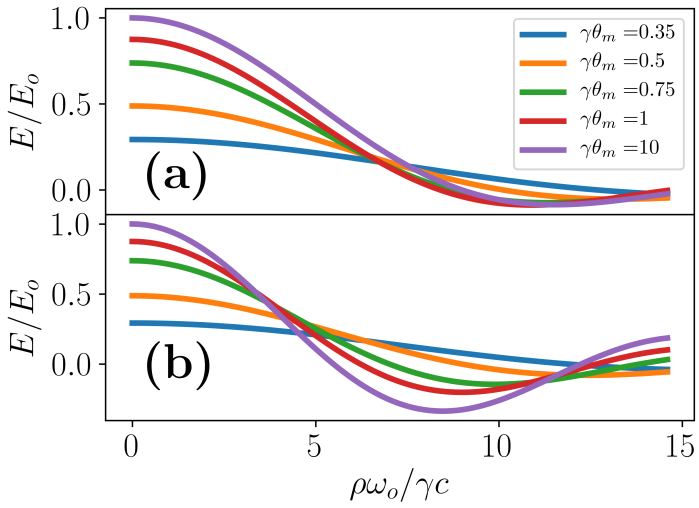

Figure 3.3: Dependence of electric field in the transverse plane at the focal point (a) in the horizontal plane $\phi'' = 0$ (b) the vertical plane $\phi'' = \pi/2$

Performing the integration over ϕ yields

$$E_x(\rho'', \phi'') = \frac{8e\gamma^6\theta_e}{c^2}\int_0^{\theta_m}\left(J_0\left(\frac{\rho k_o\theta}{1+(\gamma\theta)^2}\right) + (\gamma\theta)^2 J_2\left(\frac{\rho k_o\theta}{1+(\gamma\theta)^2}\cos(2\phi'')\right)\right)\frac{\theta d\theta}{\left(1+(\gamma\theta)^2\right)^4} \tag{3.17}$$

leaving the integration of θ can be carried out numerically. Figure 3.3 shows the relative field dependence in the transverse plane normalized by the case when $\gamma\theta_m = \infty$.

3.1.2 Arbitrary K value

Having gained some insight from considering the small K case we now develop expressions for arbitrary value of K. Unlike before we will not obtain an analytic expression for the field at the kicker center. However the only real modification will be the inclusion of a suppression factor that decreases with K for fixed angular acceptances and consequently the

kick amplitude will be found to be less than the total energy loss of the particle passing through the cooling insertion.

We start with using Eq. 3.5 with the integration variable switched to the emitter time:

$$E_\omega(\theta,\phi) = \frac{\omega(\theta)}{\pi}\int_0^{\frac{2\pi}{\omega_u}} E_x(t')\exp\big(-i\omega(\theta)t(t')\big)\frac{dt}{dt'}dt'. \tag{3.18}$$

which becomes

$$E_\omega(\theta,\phi) = \frac{4\gamma^4 e\omega_u^2\theta_e}{\pi c R_o}\int_0^{2\pi}\Bigg[F_c(\Theta,K,\tau',\phi)\times \frac{1+\Theta\big(1-2\cos^2(\phi)\big)-2\Theta K\cos(\phi)\sin(\tau')-K^2\sin^2(\tau')}{\big[1+\Theta^2+2\Theta K\cos(\phi)\sin(\tau')+K^2\sin^2(\tau')\big]^3}\Bigg]d\tau' \tag{3.19}$$

where

$$F_c(\Theta,K,\tau',\phi) = \cos(\tau')\times \exp\big[-i\tau'+i\frac{K^2\sin(2\tau')+8\Theta K cos(\phi)\cos(\tau')}{4\big(1+\Theta^2+K^2/2\big)}\big]\times \big[1+\frac{4\Theta K\cos(\phi)\sin(\tau')-K^2\cos(2\tau')}{2\big(1+\Theta^2+K^2/2\big)}\big] \tag{3.20}$$

and the variables $\Theta=\theta\gamma$ and $\tau'=\omega_u t'$ were introduced. Next inserting this expression into Eq. 3.7 yields the result

$$E_x = \frac{4\gamma^3 e\omega_u^2 K}{3c^2}F_h(K,\gamma\theta) \tag{3.21}$$

where

$$F_h(K,\gamma\theta) = \frac{3}{\pi^2}\int_0^{\Theta_m}\int_0^{2\pi}\int_0^{2\pi}\Bigg[\frac{F_c(\Theta,K,\tau',\phi)}{1+\Theta^2+K^2/2}\times \frac{1+\Theta\big(1-2\cos^2(\phi)\big)-2\Theta K\cos(\phi)\sin(\tau')-K^2\sin^2(\tau')}{\big[1+\Theta^2+2\Theta K\cos(\phi)\sin(\tau')+K^2\sin^2(\tau')\big]^3}\Bigg]d\Theta d\phi d\tau' \tag{3.22}$$

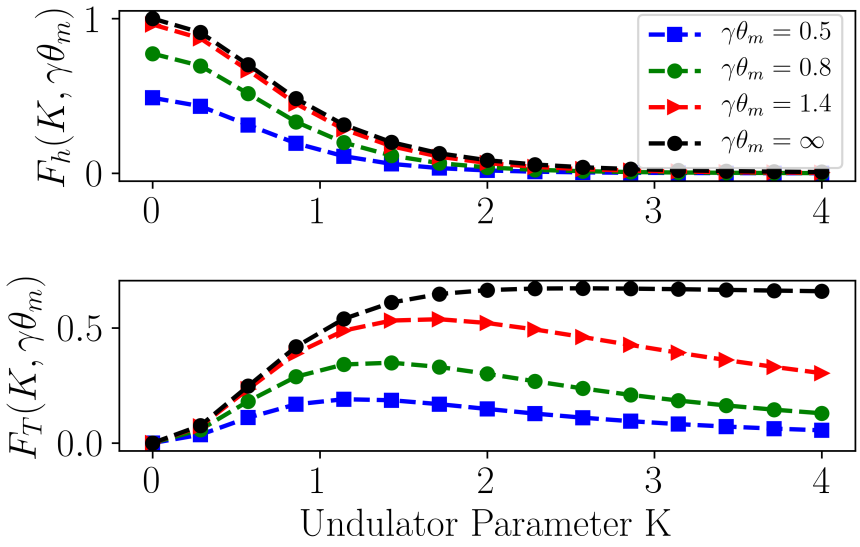

Figure 3.4: $F_h(K, \gamma\theta_m)$ and $F_T(K, \gamma\theta_m)$ as a function of K for a range of lens angular acceptances. K is varied while keeping undulator length and radiation wavelength fixed.

is the efficiency factor, $F_h(K, \gamma\theta_m) \leq 1$, mentioned before. Then the kick amplitude becomes

$$\Delta\mathcal{E} = \frac{4\pi^2}{3\lambda_o} e^2 N_u F_T(K, \gamma\theta_m) \tag{3.23}$$

where $F_T(K, \gamma\theta_m) = K^2(1 + K^2/2) F_h(K, \gamma\theta_m) F_u(\kappa)$ is the dimensionless kick amplitude per undulator period. Figure 3.4 shows $F_h(K, \gamma\theta_m)$ and $F_T(K, \gamma)$ as a function of K for various angular acceptances.

Next we consider how these formulas are guiding the choice in undulator parameters. Eq. 3.23 shows that the kick amplitude increases with shorter wavelength. On the other hand the wavelength must be chosen sufficiently long so that the high amplitude particles are not displaced too far in phase resulting in them being anti-damped. For proton or heavy ion colliders the cooling range should cover at least a few σ's where σ is the rms equilibrium size prior to cooling. Thus the wavelength is generally chosen as short as possible while still satisfying the required cooling range. Using a telescope which corrects the depth-of-field

Parameter	Value	Unit
undulator parameter, K	1.038	-
length, L_u	77.4	cm
undulator period, λ_u	11.06	cm
number of periods, N_u	7	-
on-axis wavelength, λ_o	2.2	μm
electron Lorentz factor, γ	195.69	-

Table 3.1: Undulator parameters for the OSC test in IOTA with 100 MeV electrons.

parameter, symbol	value	units
E_x	11.8	V/m
$F_h(1.03, 0.8)$	0.24	-
$F_u(0.17)$	0.91	-
$\Delta\mathcal{E}$ (max)	22	meV
x_o/y_o	590/470	μm

Table 3.2: Obtained values for OSC using the undulator parameters from Table 3.1.

effect (see section 3.2) makes the kick amplitude grow linearly with undulator length and thus should be made as long as possible for the given allocated space for a cooling insertion. This leaves K or equivalently N_u to be varied as a free parameter. From the bottom pane in Figure 3.4 we see that for finite lens acceptances growth of $F_T(K, \gamma\theta_m)$ saturates at moderate values of the undulator parameter ($K \leq 2$). At even larger K values $F_T(K, \gamma\theta_m)$ begins to decrease but for a fixed undulator length this reduction is offset by an increased number of periods leading to a leveling off of the kick amplitude for large K.

For a proof-of-principle demonstration of the OSC using medium energy electrons a large K has the detrimental effect of spoiling the equilibrium beam emittance (prior to cooling) since dispersion at both the pickup and kicker is needed for horizontal cooling. Low equilibrium emittance is desirable as it makes it possible for the OSC to be done at a short wavelength while still having acceptable cooling ranges and a reasonable optical delay to accommodate an optical amplifier. Based on these considerations a value of $K = 1.03$ was selected for the OSC in the IOTA ring. Table 3.2 compiles values related to the electric field and kick

amplitude for the undulator parameters given in Table 3.1.

3.2 Depth of field correction with a three-lens telescope

The above results were obtained for the condition that $R_o \gg L_u$. Under this assumption light emitted at a specific longitudinal location in the pickup is automatically refocused to the corresponding location in the kicker; and thus the field amplitude may be considered constant along the length of the kicker. In an accelerator the condition $R_o \gg L_u$ can not be achieved. Instead, a telescope with a transfer matrix $\mathbf{M}_T$ from pickup to kicker centers equal to $\pm\mathbf{I}$ where $\mathbf{I}$ is the identity matrix, can be used. In this case the transfer matrix between emitting and receiving points is $\mathbf{O}(l)\mathbf{M}_T\mathbf{O}(-l) = \pm\mathbf{I}$ where $\mathbf{O}(l)$ is the transfer matrix of a drift and l is a displacement measured from pickup/kicker center.

The simplest telescope for the the $+\mathbf{I}$ case requires lens placement and strengths given by:

$$F_1 = \frac{L_1 L_2}{L_1 + L_2} \qquad F_2 = \frac{L_2^2}{2(L_1 + L_2)} \tag{3.24}$$

where $2(L_1 + L_2)$ is the distance from pickup to kicker centers, F_2 is placed at the midpoint of the cooling insertion and the F_1 lenses are placed on both sides of F_2 at a distance L_2 away. In the case of the transfer matrix equal to $-\mathbf{I}$ we have

$$F_1 = L_2 \qquad F_2 = -\frac{L_2^2}{2(L_1 - L_2)}. \tag{3.25}$$

For a passive OSC test in IOTA the $-\mathbf{I}$ telescope matrix is chosen [5] and the lens focal lengths and positions are given in Table 3.3.

For active cooling the telescope has the additional requirement of tight focusing of the pickup radiation in the amplifier. For this case the $+\mathbf{I}$ telescope must be used. In passing we note that by setting $L_1 = L_2$ in Eq. 3.25 the center lens can be eliminated. This telescope would be desirable to use as the weaker focusing lenses would reduce chromatic effects. It however cannot be used in IOTA as it would place the lenses in the path of the particle beam.

symbol	value	units
L_1	143	cm
L_2	32	cm
F_1	32	cm
F_2	4.6	cm
$\gamma\theta_m$	0.8	-
Outside lens radius	5.8	mm

Table 3.3: Geometrical parameters of lens telescope for passive test of the OSC in IOTA.

3.3 Focusing error

We now consider two sources of errors: (1) manufacturing errors of the telescope lenses, and (2) lens chromatacity which plays significant role due to the wide bandwidth required for the OSC. To simplify the problem we consider these errors separately.

[5] Such choice is supported by smaller focusing chromaticity and also results in smaller transverse separation between radiation and particle in the kicker undulator. For chosen IOTA beam optics this condition is fully satisfied for horizontal plane while only partially for the vertical plane.

3.3.1 Focal length error

We first consider the case of a single-lens with $K \ll 1$ and the appropriate conditions for the depth-of-field to be ignored. Recall that in order to get to Eq. 3.12 the argument in the exponential was dropped under the assertion that all rays take the same amount of time to go from emitted to focused points. An error in the focal length introduces an additional phase term, $\Phi(\theta)$, spoiling the constructive interference of the field at the focal point and Eq. 3.12 is modified as

$$E_x = \frac{8e\gamma^5\omega_u^2 K}{c^2}\left|\int_0^{\theta_m} \exp\left(i\Phi(\theta)\right)\frac{\theta d\theta}{\left(1+(\gamma\theta)^2\right)^4}\right|. \tag{3.26}$$

Let's consider a focusing error δF so that the phase advance of the wave through the lens is given by

$$\frac{k(\theta)\rho^2}{2(F+\delta F)}. \tag{3.27}$$

For radiation emitted in the fundamental frequency and taking $K \ll k(\theta) = k_o/(1+\gamma^2\theta^2)$. The lens is located at a distance $2F$ from the pickup center and therefore $\rho \approx 2F\theta$. Then assuming $\delta F/F \ll 1$ so that a Taylor expansion may be performed to yield an expression for the phase-correction

$$\Phi(\theta) = -\frac{2k_o\theta^2\delta F}{1+(\gamma\theta)^2}. \tag{3.28}$$

Figure 3.5 shows the relative reduction in the field at the focal point as a function of δ_F for a variety telescope angular acceptances. For example if $\gamma\theta_m = 0.8$ then in order to have the field reduced by no more than 2% from focusing errors we require $\delta F < 1.23$ cm.

In order to apply this result to the telescope we will relate the error in the focal length δf

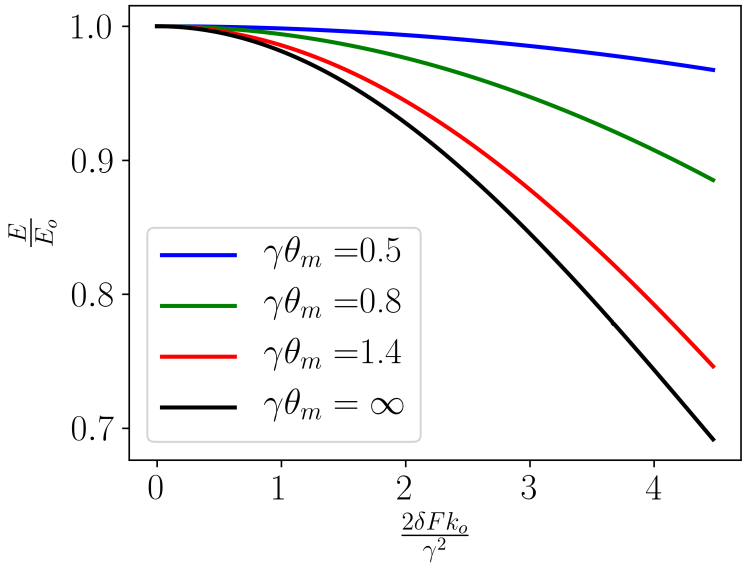

Figure 3.5: Dependence of relative cooling rate on the dimensionless focusing error for different acceptances of lens telescope.

to a displacement of the location of the focus δs. The $ABCD$ transfer matrix from pickup to kicker center is

$$\boldsymbol{M} = \begin{bmatrix} 1 & 2F \\ 0 & 1 \end{bmatrix} \begin{bmatrix} 1 & 0 \\ \frac{-1}{F+\delta F} & 1 \end{bmatrix} \begin{bmatrix} 1 & 2F \\ 0 & 1 \end{bmatrix}. \tag{3.29}$$

After multiplying and once again Taylor expanding we get

$$\boldsymbol{M} \approx \begin{bmatrix} -1 & -4\delta F \\ \frac{-1}{F} & -1 \end{bmatrix}. \tag{3.30}$$

Now consider a ray originating on-axis in the pickup center with an angle θ_o, $\boldsymbol{x}_o = (0, \theta_o)$ then in the kicker center $\boldsymbol{x}_f = \theta_o(x_f = M_{12}, \theta_f = M_{22})$. Then clearly from Fig. 3.6 $\delta_s = -M_{12}/M_{22} = -4\delta F$, and in order to have a field reduction lower than 2 % requires $|\delta s| \leq$ 4.92cm

Next going to the telescope we let each lens have some relative error $\delta F_i/F_i = f_i$. Multiplying out matrices for the telescope transfer, and keeping only terms linear in f yields

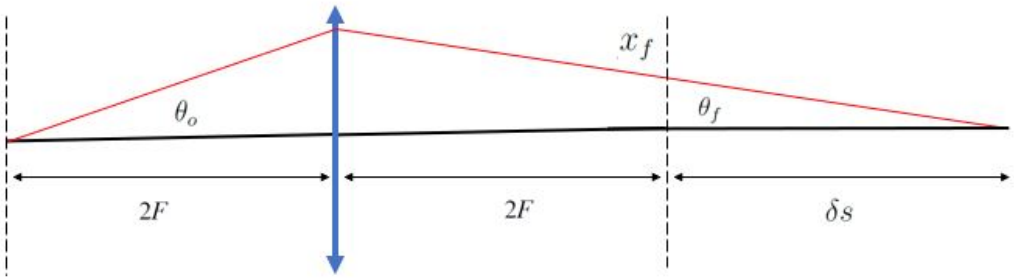

Figure 3.6: Diagram for relating a focusing error δF to a displacement of the focal length δs.

$$M_{12} \approx -2(L_1 - L_2)f_2 + \frac{L_1^2}{L_2}(f_1 + f_3) \qquad M_{22} \approx -1 \tag{3.31}$$

Then once again requiring $|\delta s| \leq 4.92$ cm and considering error in each lens one at a time only results in $|f_1| = |f_3| \leq 0.8\%$ and $|f_2| \leq 2.3\%$. A similar treatment of lens placements results in the error between the central and an outer lens $\delta L_2 \leq 2.3$ mm again assuming only one lens is displaced at a time. Note that due to the point-to-point imaging of the telescope a longitudinal displacement of the center lens (relative to the undulators) results in no error.

3.3.2 Chromatic aberration

Chromaticity in the lens results in mis-focusing of the radiation in the kicker. The lens focal length depends on wavelength, through the index of refraction $n(\lambda)$ as $F = F_o(n_{opt} - 1)/(n(\lambda) - 1)$, where n_{opt} is index of refraction at λ_{opt}, the wavelength for which the lens are designed to minimizes the telescope focusing errors. Intuitively λ_{opt} will be in the middle of the OSC band (2.2-3.2 μm) and we choose $\lambda_{opt} = 2.6$ μm. Later on in Section 4.2.4 we

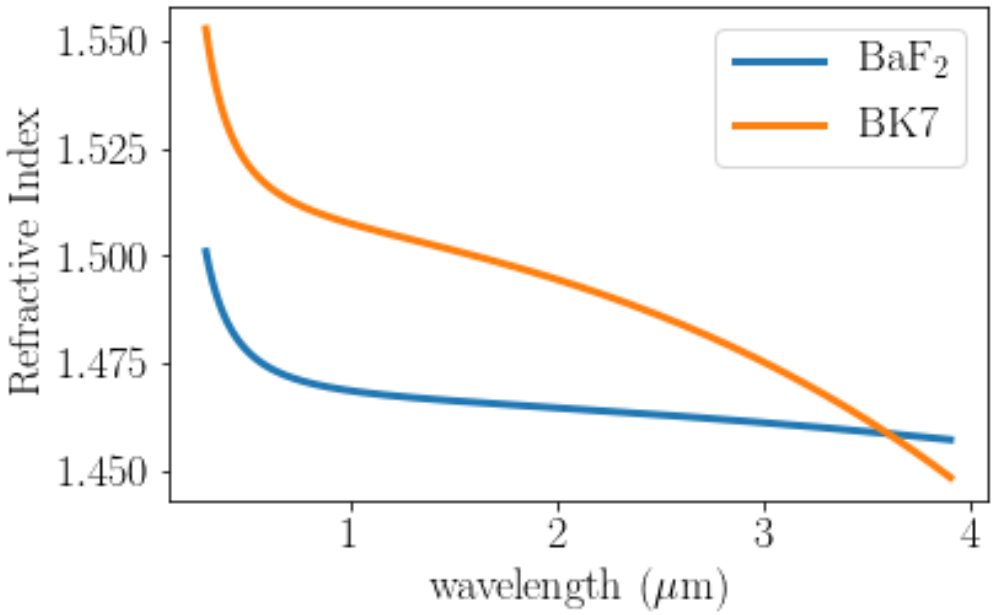

Figure 3.7: The refractive index of BaF_2 and BK7 glass.

will confirm this choice with simulations. The index of refraction for most glasses can be described well using Sellmeier's formula [22]

$$n(\lambda)^2 = 1.33973 + \frac{0.81070\lambda^2}{\lambda^2 - 0.10065^2} + \frac{0.19652\lambda^2}{\lambda^2 - 29.87^2} + \frac{4.52469\lambda^2}{\lambda^2 - 53.82^2}. \tag{3.32}$$

Where in the latter equation the empirically determined coefficients are for Barium-Flouride (BaF_2) glass and are valid over the wavelength range 0.15-15 μm. BaF_2 was chosen as the lens material for the case of 2.2 μm cooling in IOTA because of its small first order, $dn/d\lambda$=-0.00321 μm^{-1} and second order (group velocity dispersion or GVD) of -9.7405 fs^2/mm dispersions. The index of refraction of BaF_2 glass is plotted in Fig. 3.7, for comparison borosilicate glass (Schott BK7), which is commonly used for lenses, is also plotted to demonstrate the low dispersion of BaF_2. The elements of the transfer matrix can now be computed as a function of wavelength so that $\delta s(\lambda) = M_{12}(\lambda)/M_{22}(\lambda)$. This results in a focal displacement of 3 cm

for 2.2 μm light and -4 cm for 3.1 μm light. We can relate the focal length displacement to an increase in the spot size as

$$r(\lambda) = \sqrt{\frac{W_{xo}^2 + W_{yo}^2}{2} + \left(\theta_m \delta s(\lambda)\right)^2} \tag{3.33}$$

where W_{xo} and W_{yo} are the horizontal and vertical beam sizes computed from Eq 3.17. To first order the electric field will be inversely proportional to $r(\lambda)$ resulting in a 2 and 4 % decrease in the field amplitude for 2 and 3.1 μm light respectively. Based on this criteria we do not expect chromatic effects to make a significant contribution to the kick amplitude. These results are confirmed in Section 4.2.4.

CHAPTER 4

NUMERICAL MODEL OF THE ENERGY EXCHANGE BASED ON A WAVE-FRONT PROPAGATION CODE

In the previous chapter we developed a semi-analytic theory of the kick amplitude. Here we present simulations using Synchrotron Radiation Workshop (SRW) and to benchmark this work simulation results are first compared to the case considered in theory (i.e. a single focusing lens with depth of field suppressed by a large separation of undulators compared to their lengths). Finding acceptable agreement between theory and simulation we go on to test the telescope and finally consider chromatic effects which occur due to the wide radiation-band that the OSC requires.

4.1 Synchrotron Radiation Workshop

Synchrotron Radiation Workshop (SRW) was first released in the late 1990's and provides computational tools which are useful for typical applications of synchrotron radiation [23] [24] [25]. For example the radiated flux in an undulator can be efficiently computed and once generated, the radiation field can be propagated through many typical optical elements found in beam-lines such as mirrors, apertures and diffraction gratings. Part of SRW's computation efficiency stems from doing these two tasks, emission and then propagation of the radiation field, with two different methods.

Computation of the emission of the radiation field is done in the near-field and is based on the

Fourier-transformed retarded scalar and vector potentials. The field is found by numerically evaluating

$$\boldsymbol{E}_1 = ie\frac{\omega}{c}\int_{-\infty}^{\infty}\frac{\boldsymbol{\beta}-\boldsymbol{n}(1-\frac{ic}{\omega})}{|\boldsymbol{r}-\boldsymbol{r'}|}\exp\big(i\omega/c(c\tau+|\boldsymbol{r}-\boldsymbol{r'}|)\big)d\tau \tag{4.1}$$

where ω is the field frequency, as before $c\boldsymbol{\beta}(\tau)$ is the particles instantaneous velocity at the emitter time τ, $\boldsymbol{n}(\tau)$ is the unit vector pointing from the particle to the observation point a distance $R(\tau) = |\boldsymbol{r}-\boldsymbol{r'}|$ away. Once evaluated the propagation of a transverse component of the field obtained above is done with standard scalar-diffraction theory from Fourier optics where

$$E_{\perp 2} = \frac{\omega}{2\pi ic}\int_{\Sigma}\frac{E_{\perp 1}}{|\boldsymbol{r}-\boldsymbol{r''}|}e^{i\omega|\boldsymbol{r}-\boldsymbol{r''}|/c}d\Sigma \tag{4.2}$$

where again Σ is the surface from which the field is diffracting from to the observation point a distance $|\boldsymbol{r}-\boldsymbol{r''}|$ away. In SRW the wavefront is discretized over a rectangular grid with the spatial dimensions and number of points determined by the user. During the propagation the user can select options to resize the grid to maintain or modify the wavefront resolution as desired. Generally in our simulations any resizing options were turned off.

It is worthwhile to compare this equation to Eq. 3.7 where there is only one substantial difference: in the analytic theory the electric field comes from the discrete Fourier coefficients of the time domain field and assigned a one-to-one relationship between observation angle θ and field frequency. In doing this we only compute the amplitude of the field and when necessary tack on in an ad hoc fashion a longitudinal dependence, $\sin(\omega_o t + k_o z)$ tacitly implying a pulse of infinite length. In SRW this is not the case which enables us to observe the temporal shape of the undulator wave-packet along with its modulation through the kicker. With this in mind we would like to emphasizes that the formulas presented in Chapter 3 were done in the time domain yet SRW computations are done in the Fourier-plane. Therefore to make a comparison to theory, SRW outputs are inverse fourier-transformed into the time domain using an fft algorithm. Fig 4.2 shows the undulator wave-packet for a single classical-

electron. To the best of our knowledge constructing the undulator wave-pulse in the time domain is a novel application of SRW implemented in the course of our research.

On the top panel of Fig. 4.1 the on axis and integrated intensity spectrum is shown for

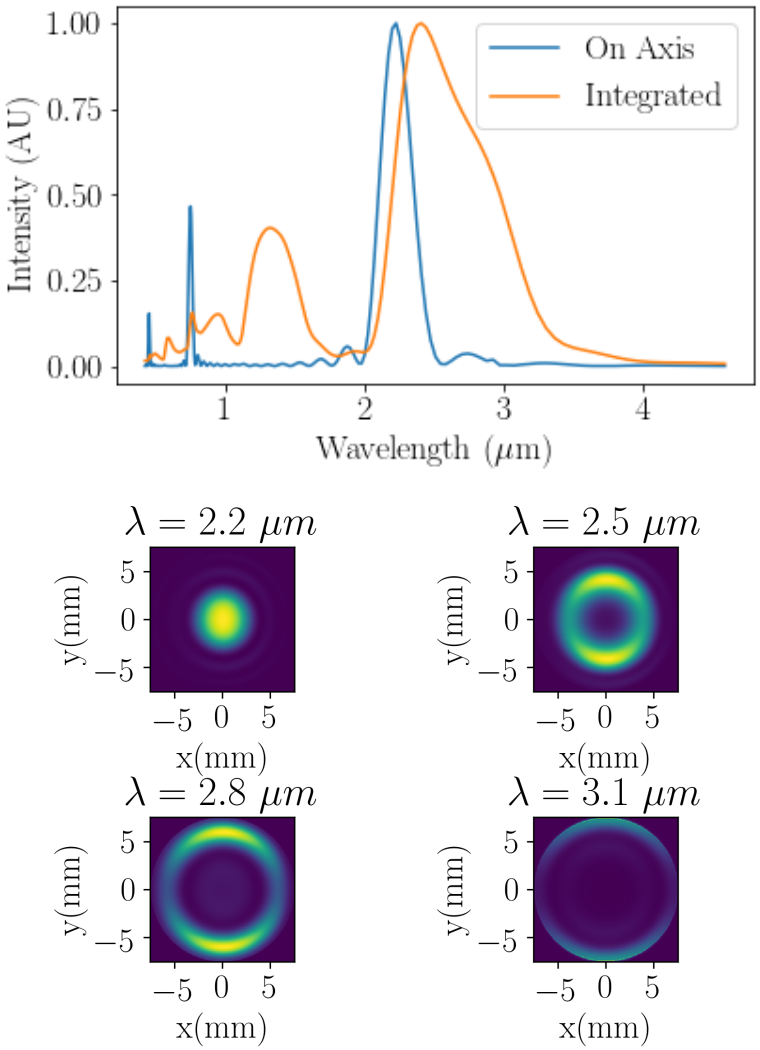

Figure 4.1: Top pane: The on axis and integrated intensity for an undulator with the parameters expected in IOTA. Bottom pane: Transverse Intensity at various wavelengths in the fundamental harmonic.

the undulator parameters expected in IOTA. The right side shows the transverse intensity

patterns for various wavelengths in the first harmonic and we see agreement with the standard formula,

$$\lambda_l = \frac{\lambda_u}{2\gamma^2}\left(1 + 1/2K^2 + (\gamma\theta)^2\right) \tag{4.3}$$

related the radiation wavelength λ_l to the observation angle. A circular aperture corresponding to $\gamma\theta_m = 0.8$ was used for all figures.

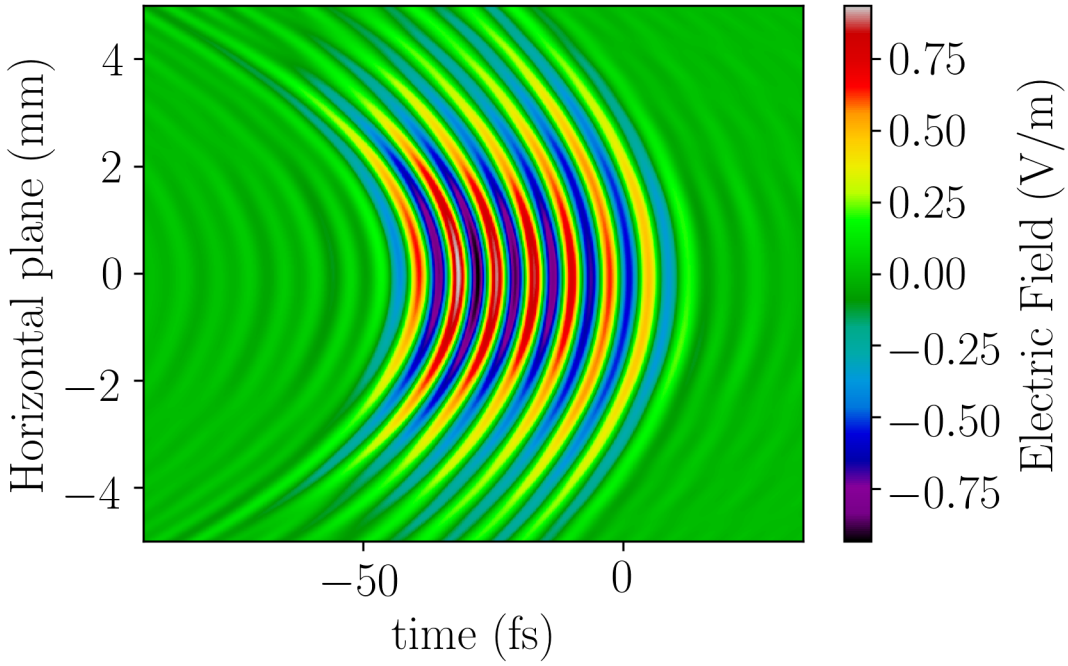

Figure 4.2: The time domain pulse, in the horizontal plane approximately 90 cm from the exit of the pickup undulator, computed with the outputs of SRW for the 2.2 μm OSC in IOTA.

4.2 Simulations of the OSC kick amplitude for IOTA 2.2 μm test

4.2.1 Electric field amplitude for a single-lens with suppressed depth of field

To benchmark our SRW code we consider the case of a single-focusing lens with the distance from pickup to kicker centers, $L_t = 19.5$ m much greater than the undulator length, $L_u = 0.77$ m [26]. In which case the electric field in the kicker is given by Eq. 3.21. In order to scan K the undulator B-field and period were varied while keeping the on-axis wavelength and length fixed. Additionally separate cases of the lens's angular acceptance were computed. The distance from pickup center to focusing lens was used to define acceptances. A wave-packet is formed in the kicker center and the maximum of its absolute value is interpreted as the amplitude.

The results are plotted in Fig. 4.3. We see good agreement between theory and simulation

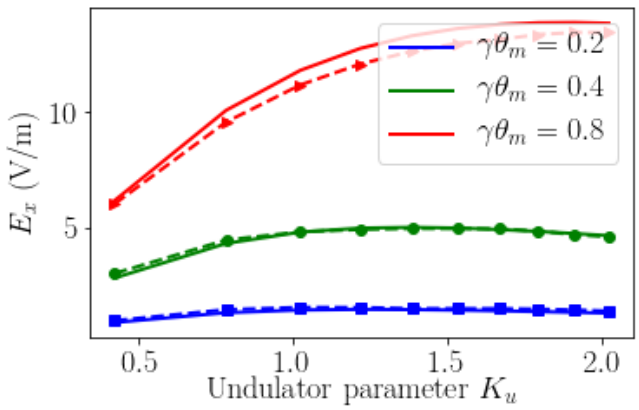

Figure 4.3: Comparison of the electric field at the focus on a single lens analytically computed (solid traces) and simulated with SRW (symbol with dashed traces) for the same cases of angular acceptance.

with a maximum discrepancy of 5 %.

4.2.2 OSC kick with telescope

At the end of Chapter 3 it was noted suppression of the depth of field by simply placing undulators far apart is not practical in an accelerator. Instead a three-lens telescope was suggested. To test the effectiveness of this telescope we will first re-compute the electric field in the kicker center for the undulator and lens parameters expected in IOTA. From theory $F_h(1.03, 0.8) = 0.25$ and using Eq. 3.21 yields a value for the electric field amplitude of 11.8 V/m while the value we find using SRW is 10.9 V/m or approximately a 7% discrepancy. Still assuming the field amplitude is fixed along the kicker using Eq. 3.23 and a value $F_u(0.18) = 0.91$ yields a kick amplitude of 22 meV from theory and 20.1 meV from SRW. Then using Eq. along with values given in Table 2.1 Going further with the SRW results we can remove the assumption of a constant electric field amplitude in the kicker. This is done by computing the undulator wave-packet at several locations (in the case of these simulations every 3.2 mm) of the kicker. We then place a test particle, phased so that the energy kick is maximum, just in front of the wave-packet at the entrance of the pickup. As was already shown the particle travels at a velocity $c\bar{\beta} = \beta(1 - \frac{K^2}{4\gamma^2})$ and so slips behind the wave-packet an amount

$$\delta_t = \frac{z(1 - \bar{\beta}) + \frac{K^2}{8\gamma^2\kappa}\sin(2k_u z)}{c} \tag{4.4}$$

where z is the particles location in the pickup. Then once the particles displacement in the time domain field is found, the electric field seen by the particle along the kicker is recorded and is shown in the lower pane of Fig. 4.4. One assumption built into this technique is that the radiation field is not modified by the interaction with the electron. In reality this is not true but is of no consequence when computing the kick amplitude and only a single particle

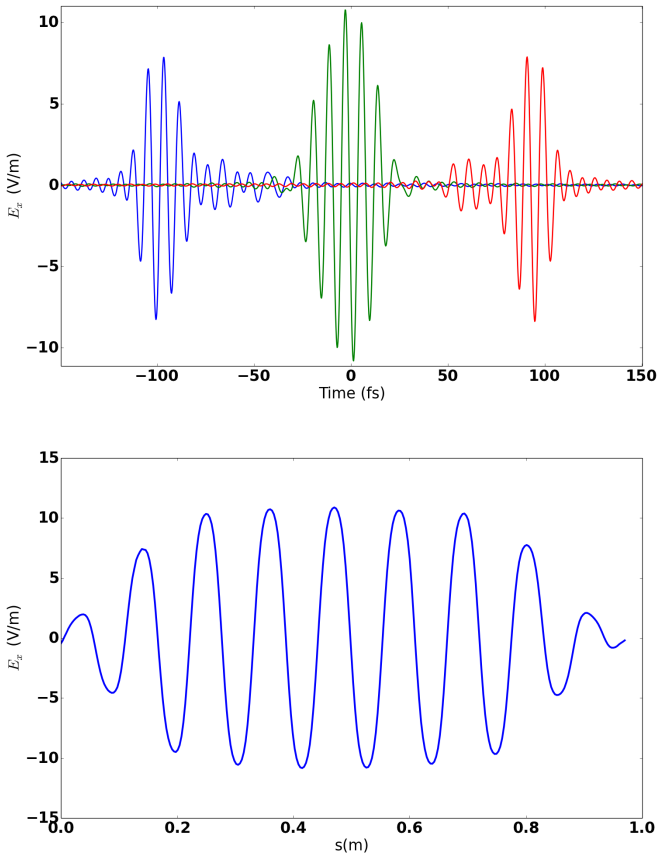

Figure 4.4: Top: The undulator wave-packet at the entrance (blue), center (green) and exit (red) of the kicker. Bottom: The electric field as seen by the electron co-propagating with the imaged pickup radiation.

is considered.

In general the time resolution of the Fourier Transform does not equal δ_t and so to find the field a linear-interpolation routine between the two nearest points was used.

In the top pane of Fig. 4.4 the undulator wave-packet is plotted, which is seen to modulate at the entrance (blue), center (green) and exit (red) of the kicker with an artificial delay added to the pulses for clarity. This modulation can be understood as follows: Near the entrance of the kicker light emitted at the entrance of the pickup is being focused while light that was emitted towards the exit of the pickup is not yet focused. Thus we see light emitted earlier

in time is largest in amplitude. At the center of the kicker radiation emitted at the center of the pickup is focused and the wave-packet looks symmetric. Finally the exit of the kicker is just the opposite case of the entrance and so light emitted at a later time is largest in amplitude. Because of the slippage just described the particle would move from left to right within the wave-packet always in the vicinity of the wave-packets peak amplitude.

In addition to the longitudinal field dependence, the reduction of the field amplitude as

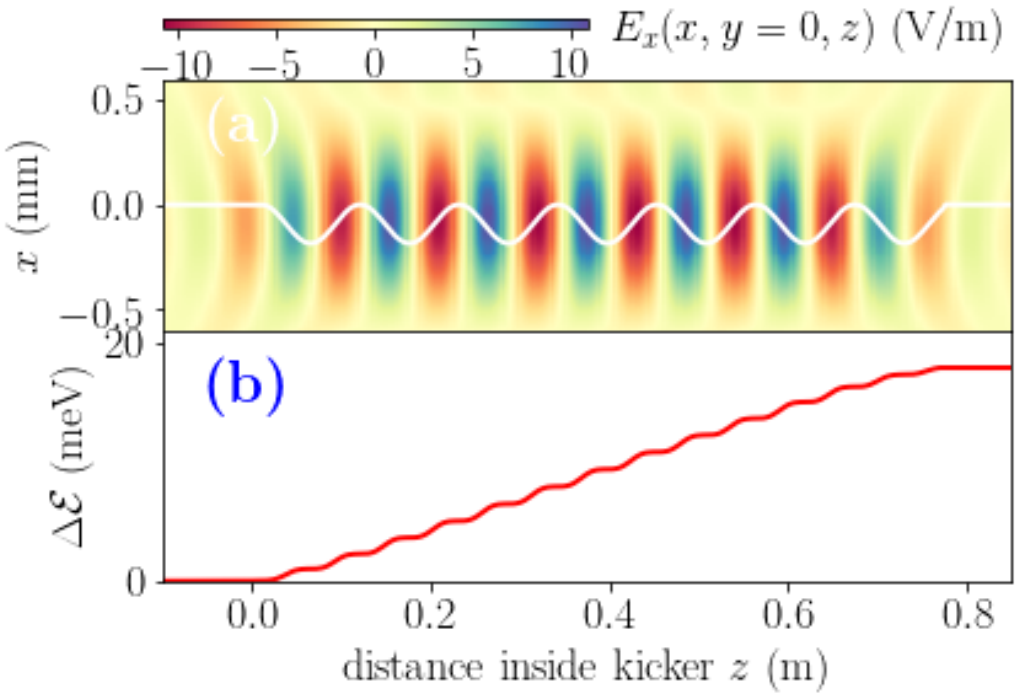

Figure 4.5: Top: The electric field imaged in the kicker in moving plane of the electron. The white trace is the electrons trajectory (a). Bottom: The energy gain of the particle passing through the kicker and phased for maximum gain(b).

the particle moves off axis during its oscillation can be accounted. Finally the kick value is computed by numerically integrating

$$\Delta\mathcal{E} = e\int_0^{L_u} E(x,z)v_x(z)dt. \tag{4.5}$$

A cumulative sum of $\Delta\mathcal{E}$ is shown on the bottom of Fig. 4.5. Accounting both dependencies the kick amplitude is found to reduce by 10.4 % to 18 meV. The majority of this loss comes from the longitudinal dependence. Although the telescope does address the depth of field issue in terms of focusing the radiation, the effective angular aperture of the lenses for light that is emitted away from the pickup center is reduced. In Fig 4.4 a fading at the entrance and exit of the kicker can be seen.

Including the transverse dependence of the field accounted only a 1 % loss in the kick amplitude. For the undulator parameters for 2.2 μm OSC transverse amplitude of motion of the the particle is 93 μm. At this extent the electric field has reduced by 5 %. However coupling between the particle and radiation field is achieved through v_x which is zero at the particles furthest extent and maximum as the particle goes through the optical axis (where the field amplitude is maximum). It was therefore within our expectation that the transverse field dependence would make at most a minor correction to the kick amplitude.

The top pane of the right side of Fig 4.4 shows the electric field in the x-z plane, the white line shows the particles trajectory through the kicker. The bottom pane shows the particles energy gain.

4.2.3 OSC sample-slice length

The entire purpose (and only advantage) of the OSC over ordinary stochastic cooling is a reduction in the incoherent heating effect which stems from overlapping particles leading to faster damping times and consequently a lower equilibrium emittance. By varying the arrival time, t_a, of the particle entering the kicker undulator (relative to the wave-packet) the kick value as a function of particle delay, $\Delta\mathcal{E}(t_a)$, can be computed. Or imagining our

test particle arrives at the same time, t_a can also be re-interpreted as the arrival time of neighboring particles thus giving us a measure of the sample-slice length. In the case of IOTA the transverse size of the wave-packet is larger than the beams (590 μm to the beams 240μm at 1 σ in the horizontal plane) and therefore slices are only made longitudinally. If a Gaussian envelope, $w(t_a)$, is fitted over $\Delta\mathcal{E}(t_a)$ then the number of particles per sample-slice is approximately

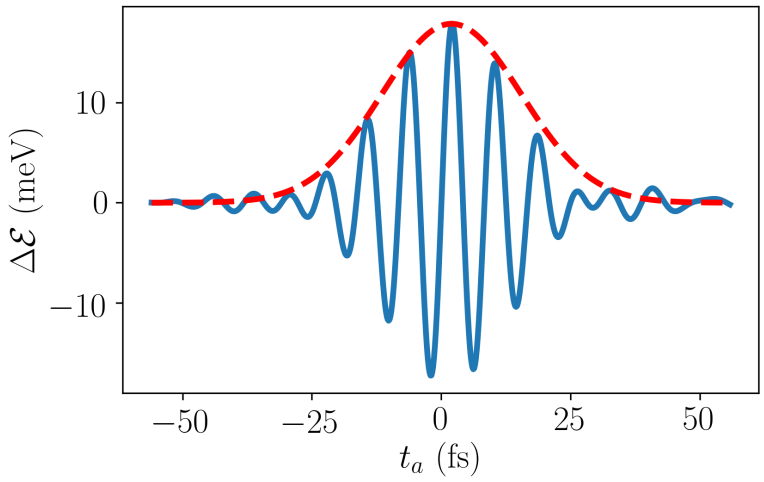

Figure 4.6: The kick value as a function of particle arrival time, t_a (blue) and its envelope, $w(t_a)$ (red).

$$N_s \simeq \frac{cN}{l_b}\int w(t_a)dt_a = \frac{Nc\sigma_{t_a}\sqrt{2\pi}}{l_b}. \tag{4.6}$$

For the 2.2 μm OSC case in IOTA $l_b = 14.2$ cm (prior to cooling), σ_{t_a} was found to be 13.5 fs yielding $N_s/N = 7 \times 10^{-5}$. Or in other words a sample slice is approximately 4 μm which corresponds to a beam with $N = 10^6$ particles (as expected for test in IOTA), $N_s \approx 70$ particles. It is interesting to note that common approximation to the undulator wave-packet length is $N_u\lambda_o/c = 51.3$ fs which is quite a bit longer than the σ_{t_a} computed from simulations. The source of this discrepancy is the modulation of the wave-packet already

discussed. Because only radiation from a few of the undulator periods are in focus at any one point, the effective length of the wave-packet becomes shorter.

4.2.4 Chromatic effects in SRW

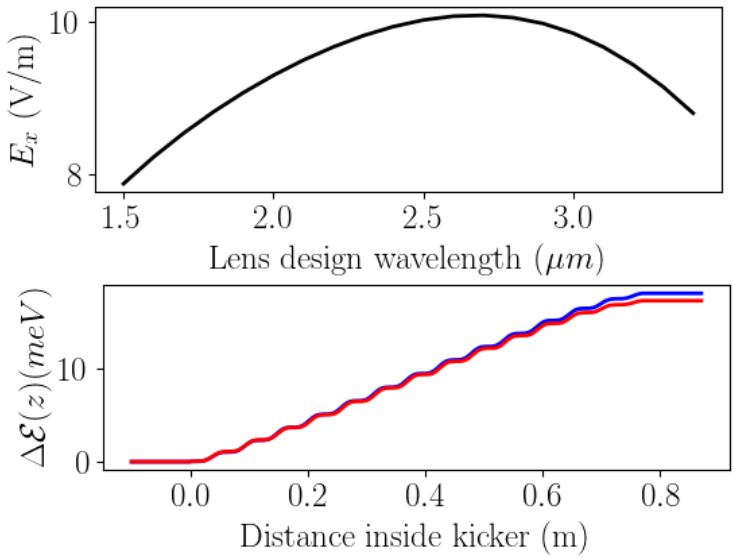

Figure 4.7: Top: The electric field amplitude at the kicker center for different design wavelengths of the telescope lenses. Bottom: The energy exchange for a particle co-propagating with the simulated radiation field from SRW through the kicker both with (red) and in the absence of (blue) lens dispersion.

In chapter 3 we estimated the effect of lens chromaticity by computing the displacement of the focal length as a function of radiation wavelength and relating this to an increase in the radiation spot size. It was suggested that there would be some optimal wavelength, somewhere in the middle of the OSC band, for which the lenses should be designed to minimize focusing errors. Because the propagation of the radiation field through the optics is done in the Fourier-plane it is relatively straightforward to include chromatic effects in our simulations.

As before the index of refraction is computed using Sellmeier's formula. Then at each radiation wavelength the lenses focal length's are varied while keeping the radii of curvature fixed. In order to find the optimal wavelength we can then do this computation over a range of fixed lens curvatures and compare the field amplitude as is shown in the top pane of Fig. 4.7 confirming the choice of $\lambda_{opt} = 2.6\ \mu$ m. In the bottom pane the energy exchange for the particle receiving the maximum kick is shown with and without chromatic effects. We see a decrease in the kick of about 4 % in agreement with previous estimates. Note that in addition to lens chromaticity the SRW results also include the effect of pulse lengthening from GVD.

4.3 Higher harmonics and the OSC

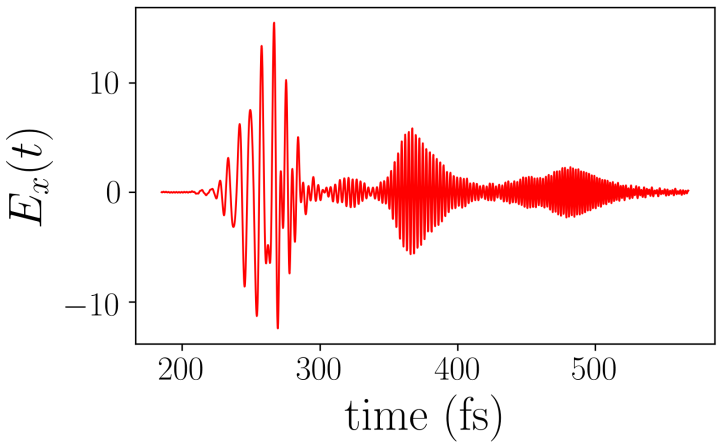

Figure 4.8: Time domain electric field in the kicker center with radiation computed through the 3rd harmonic.

Although the undulators have a modest value for $K = 1.03$ there is already a significant amount of radiation in the higher harmonics as was seen in Fig. 4.1. In Chapter 3 only the

fundamental was considered in deriving the kick amplitude. There are two justifications for this which we can verify using SRW. The first is that second order dispersion of the glass making up the lenses results in temporal separation between the harmonics. In Fig. 4.8 this was demonstrated by computing the time domain field in the kicker center and including radiation up through the 3rd harmonic.

The second reason, at least for the case of the 2nd harmonic, is that the imaged pickup radiation in the kicker does not appear on axis. This is shown in in Fig. 4.9 where radiation from all harmonics but the 2nd (i.e. radiation from 1.1 to 2.2 μm) was filtered, the electric field in the moving plane of the electron in the kicker is shown. Again since the rate of energy exchange between the electron and field is proportional to v_x which reaches its maximum on axis where the field reduces to zero the exchange between the particle and 2nd harmonic is very small.

It is also interesting to observe the electric field in the moving plane of the particle when harmonics up through the 3rd are included and dispersion in the lenses has been turned off so that constructive interference of all harmonics can take place in the kicker. From Eq. 3.1 we infer that the instantaneous rate of radiation emission is proportional to the particles acceleration, which in an undulator occurs when the particle reaches its maximum transverse off set. Therefore when the radiation is imaged in the kicker in the moving frame of the electron we expect to see 'hot-spots' as the electron is turning around which are clearly seen in the bottom pane of Fig. 4.9.

4.4 Single-lens passive OSC

The analytic theory presented in Chapter 3 first assumed a single-lens with the undulators far apart in order to suppress the depth-of-field effect. It was then suggested a 3-lens telescope

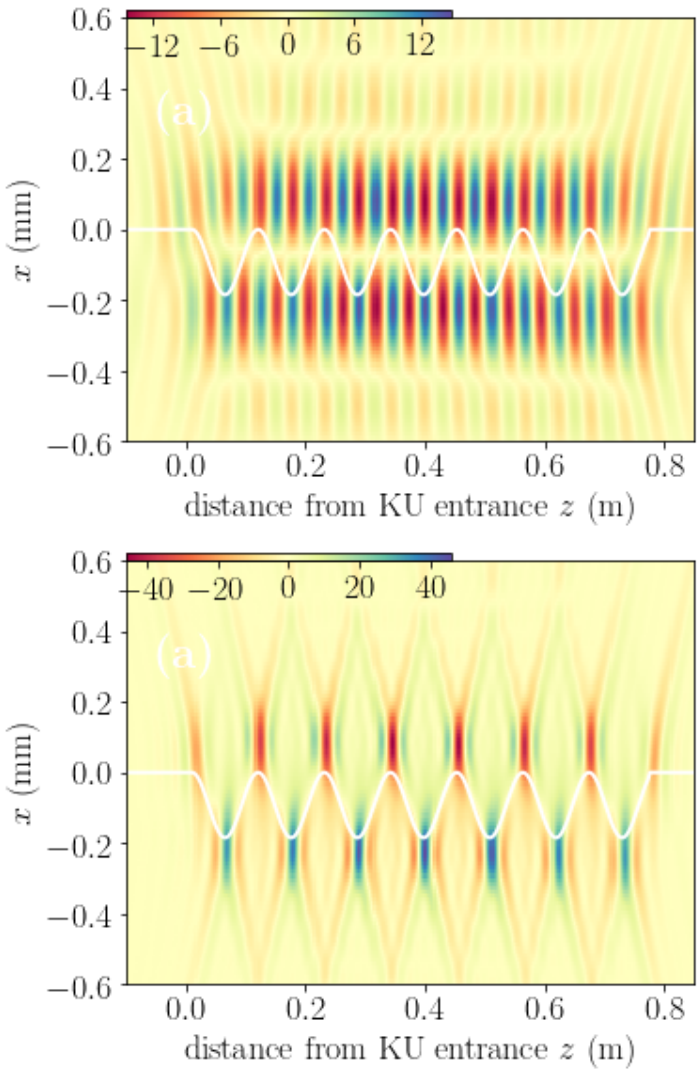

Figure 4.9: Left: Imaged radiation of the isolated 2nd harmonic in the electron's moving frame through the kicker. Right: Radiation up through the 3rd harmonic with lens dispersion turned off. Radiation 'hot-spots' form where the particle turns around in the transverse plane.

could be used as a practical fix for the depth-of-field. A surprising result from the simulations presented in this chapter is, if a single focusing lens is used in place of a telescope[1] then they both have essentially the same kick value!

This result can be understood as follows: the depth of field is not addressed for a single-lens

[1]the distance between undulators is the same, as determined by the space constraint in IOTA, and both systems have the same angular acceptance and therefore the single lens requires a larger aperture

but this results in over-focusing of the wave-packet in the first half of the kicker leading to an approximately 20 % increase in the field amplitude (see Fig 4.10). This compensates the under-focusing in the second half of the kicker. Additionally, in terms of optics considerations the single lens enjoys two advantages over the telescope (i) A weaker focusing lens implies a reduction in chromatic effects and (ii) since there is only one surface for the light to go through, loss from reflections are reduced. This latter effect is not accounted for in simulations. Even so we find that the single-lens slightly outperforms the telescope (16.7 meV to 16.5 meV) in kick amplitude. $\Delta\mathcal{E}(z)$ is plotted for the single lens and telescope cases. It is seen that the single-lens results in a much less uniform kick but yields essentially the same kick value.

The realization that a single-lens setup works just as well as the telescope has made a tremendous impact on the OSC project in IOTA. First mounting a single-lens is considerably more simple than the telescope. A relatively straight-forward optical stage to allow for transverse position and tilt correction (vertical and horizontal) can be used. For a telescope the lens positions and tilts were to be per-aligned on an optics bench and made fixed. Then inside vacuum the entire telescope as a whole would be aligned with the same degrees of freedom as the single-lens. However for the telescope a more sensitive stage capable of handling the torque applied resulting from extended nature of the telescope would be needed. Furthermore in general a single-lens is less sensitive to alignment and focal length errors.
The second benefit of a single lens is even more dramatic. The use of one lens allows for the needed optical delay or M_{56} to be reduced. This in turn allows for the radiation wavelength to be changed to 950 nm while still keeping the same cooling range. From Eq. 3.23 for fixed K we see an decrease in the radiation wavelength and an corresponding increase in N_u (from 7 at 2.2 μm to 16 for 950 nm) will result in the kick value increasing from the theoretical 22 meV to 116 meV. Although the effect of the increased kick amplitude is somewhat reduced my the smaller M_{56} when damping rates are computed (see Eq. 2.35) the

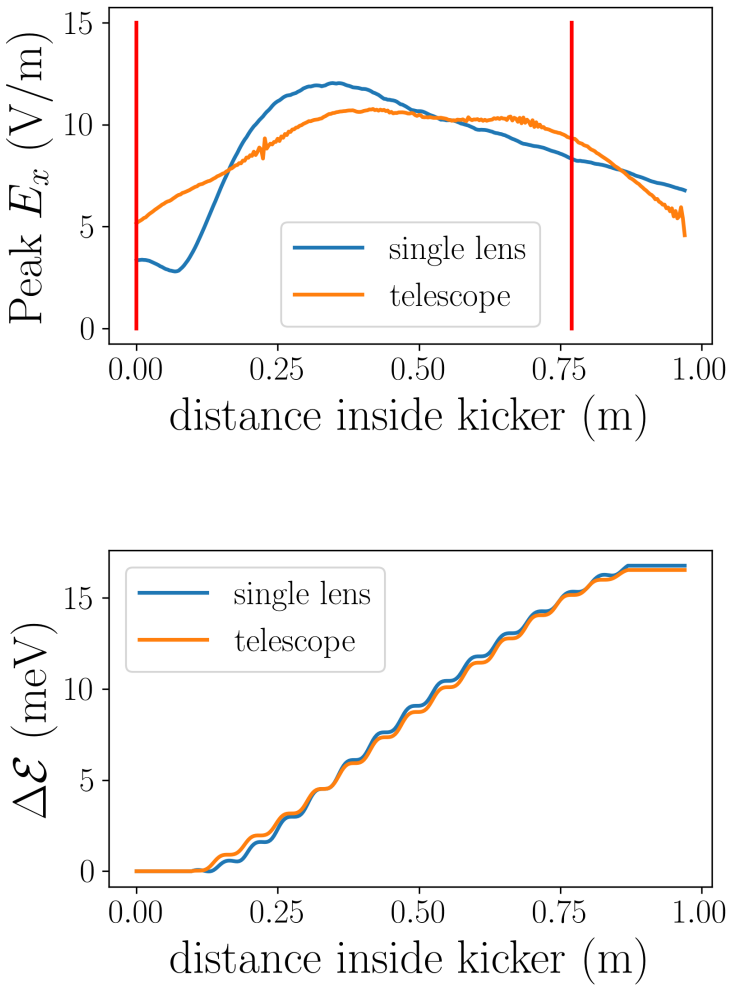

Figure 4.10: Top: The peak of the electric field along the kicker for the single lens (blue) and telescope (orange). Vertical red lines indicate entrance and exit of the kicker. Bottom:The energy gain of the electron passing through the kicker for the telescope and single lens cases.

wavelength change enabled by single-lens focusing still results in a five-fold increase in the damping rate. Additionally detectors (cameras and photo-diodes) are more sensitive and inexpensive at 950 nm making the down-stream diagnostics cheaper and easier to use. Thus the change in radiation wavelength makes for the passive test of the OSC in IOTA much

more likely to be a successful demonstration. The use of the simulation methods presented here played a major role in the wavelength change.

CHAPTER 5

AMPLIFICATION FOR OSC

In this chapter we discuss amplification in the context of OSC. An optical amplifier (OA) should have the following characteristics

- (i) High gain, G. 20-30 dB of gain is required for proton or heavy-ion cooling.
- (ii) Small optical delay of a few millimeters to ensure sufficient cooling ranges.
- (iii) A bandwidth with at least a few 10's of THz to preserve the electromagnetic wave-packet radiated in the pickup.
- (iv) capability of operating at a duty cycle equal to or greater than the accelerators (i.e. the amplifier has capability of amplifying pulses which match the length and repetition rate of the accelerators).

We should distinguish between two notions of the word 'pulse' for the OSC. The radiation arrives at the amplifier in the form of a pulse with its length determined by the longitudinal dynamics of the accelerator (i.e. the bunch length which can range from ps in light sources to ns in colliders). The second notion of a pulse is the pulse formed by a single electron (which arrives in the amplifier as a superposition of all the electrons in the bunch) we saw in Chapter 4. It carries with it considerable bandwidth which will exceed that of the amplifiers and hence be distorted. It is studied in Sections 5.1.1 and 5.2.2.

If it were not for criteria (iv) an optical parametric amplifier (OPA) would make a superb OA [27]. Unfortunately in an OPA amplification only occurs when there is both temporal and spatial overlap between the signal and pump beams. Since high intensities are needed to

drive the nonlinear response of the crystal (causing the gain), pulse energies on the order of a mJ are needed. Then since a typical accelerator operates at repetition rates greater than a few MHz this brings the required laser pumping power in excess of a KW which is beyond the capabilities of current laser technology.

Instead we consider an amplifier based on a solid-state gain medium pumped with a CW laser. With this setup the bunch length becomes irrelevant since, as we will see in the next section, the pickup radiation in the amplifier is too weak to affect the population inversion in the amplifier responsible for the gain.[1]

Recall that the desire for sufficiently large cooling ranges presented toward the end of Chapter 2 set the optical delay to 2 mm and radiation wavelength to 2.2 μm. Based on this criteria an amplifier utilizing a 1-mm-thick Chromium-doped Zinc-selenide (Cr:ZnSe) crystal was selected for the active test of the OSC in IOTA. Note that the criteria (i) and (ii) are contradictory in the sense that a shorter delay always produces a smaller gain in a solid-state amplifier. To some degree this can be counteracted by increasing the Cr dopant concentration, N_T in the ZnSe host-crystal. However for Cr:ZnSe even assuming the highest available N_T its performance is limited by (ii). Table 5.1 summarizes the relevant physical properties of Cr:ZnSe and the expected amplifier performance.

5.1 Gain equations for a single-pass amplifier

In a laser amplifier based on a solid-state gain medium light amplification is achieved by creating a population inversion (i.e. there is an excited state where the ion population density is greater than the next lowest excited state) inside the crystal. The population inversion

[1]This comment applies to the IOTA proof-of-principle experiment. For OSC with a high-luminosity TeV proton beam the total pulse energy before amplification can be on the order of nJ which at MHz repetition rates can drain the population inversion.

Symbol	Parameter	Value	Unit
λ_s	Peak fluorescence	2.45 [28]	$\mu m.$
$\sigma_s(\lambda_s)$	emission cross-section	1.3×10^{-18} [29]	cm^2
n(λ_o)	Refractive index	2.45 [28]	-
dn/dT	Slope of n with temperature	70×10^{-6} [28]	1/K
K (77 K)	Thermal conductivity	100 [30]	W/m-K
L	Crystal length	1.0	mm
N_T	Cr dopant concentration	2.0×10^{-19}	ions/cm^3
G(λ_s)	Gain	7	dB

Table 5.1: Physical properties of Cr:ZnSe and estimated gain.

required for lasing is created by some external pumping mechanism which transfers energy from an external source to the laser-gain medium. Pumping can be accomplished via flash lamps, diode arrays or even another laser [32]. Pumping based on flash-lamps include the case of Nd:Yag lasers [33] while external laser pumping is commonly implemented in Ti:Sp lasers [34]. In the case of Cr:ZnSe high power and robust thulium fiber lasers that lases in the absorption band [35] are commercially available, providing a convenient pump.

In order to calculate the single-pass gain we use a 4-level model (see Fig. 5.1) where a pump photon is absorbed in the ground state causing a transition from 0 to 3, followed by a rapid, radiation-less transition between 3 and 2. Here $i = 0, 1, 2, 3$ is used to denote association with the ith level in the medium. Stimulated emission of the signal (radiation coming from the pickup) causes a de-excitation between 2 and 1 and additionally spontaneous emission, over the amplifier bandwidth, occurs here too. Finally another rapid and radiation-less transition happens between 1 and 0 before the ion is finally back into the ground state. An added complication can occur when, as is the case for Cr:ZnSe pumped at 1908 nm, the pump lasers wavelength overlaps with the emission spectrum. In this case a transition occurs directly between 2 and 0 and results in a reduction of the population inversion responsible for the signal gain.

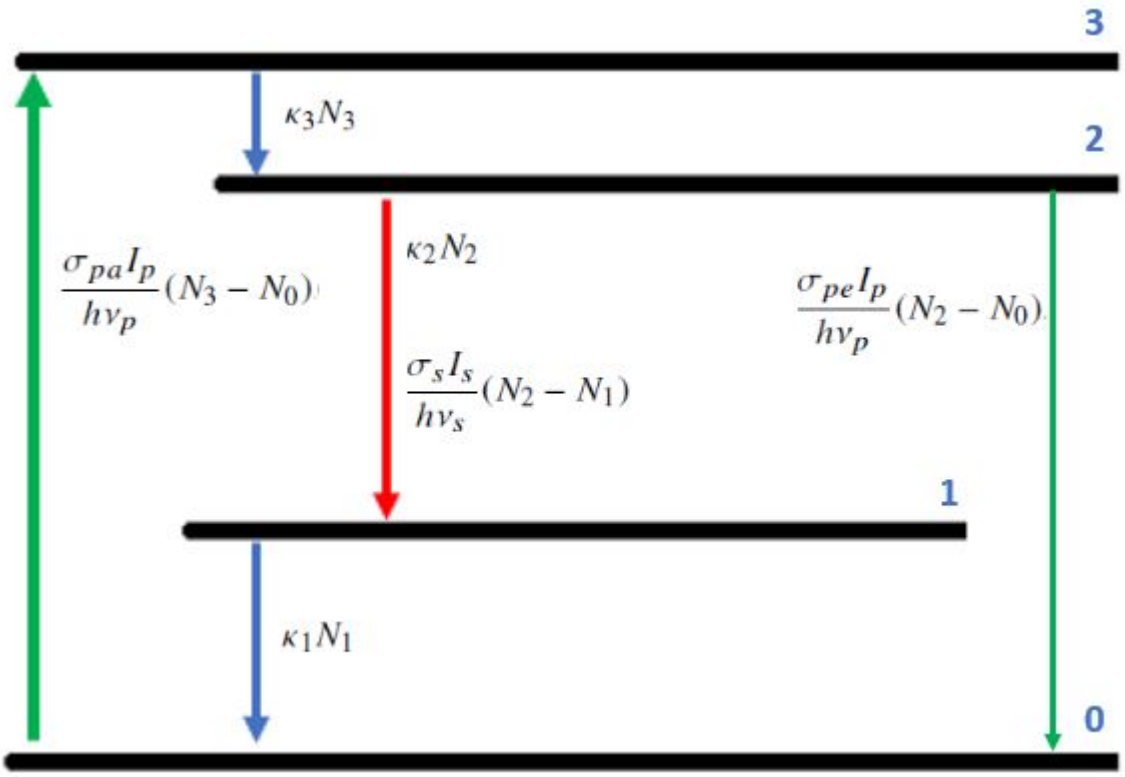

Figure 5.1: Illustration of the a 4-level pumping scheme for Cr:ZnSe. The green arrow represents transition from the pump laser while the red indicates transitions from spontaneous or stimulated emission. Blue arrows indicate radiation-less transitions.

Introducing N_i as the population density the dynamics are described by the following rate equations:

$$\begin{aligned}
\frac{dN_3}{dt} &= -\kappa_3 N_3 + \frac{\sigma_{pa} I_p}{h\nu_p}(N_0 - N_3) \\
\frac{dN_2}{dt} &= \kappa_3 N_3 - \kappa_2 N_2 - \frac{\sigma_s I_s}{h\nu_s}(N_2 - N_1) - \frac{\sigma_{pe} I_s}{h\nu_p}(N_2 - N_0) \\
\frac{dN_1}{dt} &= \kappa_2 N_2 - \kappa_1 N_1 + \frac{\sigma_s I_s}{h\nu_s}(N_2 - N_1) \\
\frac{dN_0}{dt} &= \kappa_1 N_1 - \frac{\sigma_{pa} I_p}{h\nu_p}(N_0 - N_3) + \frac{\sigma_{pe} I_s}{h\nu_p}(N_2 - N_0)
\end{aligned} \tag{5.1}$$

where $\kappa_i \equiv 1/\tau_i$ is the decay rate, I_p is the pump intensity and I_s is the signal intensity, σ_s is the emission cross section at the signal frequency ν_s while σ_{pe} is the emission cross section at the pump frequency ν_p and finally σ_{pa} is the absorption cross section at the pump frequency. The attenuation of the pump laser propagating through the crystal is given as

$$\frac{dI_p}{dz} = -I_p[\sigma_{pa}(N_0 - N_3) + \sigma_{pe}(N_0 - N_2)] \tag{5.2}$$

while the growth of the signal intensity is determined by

$$\frac{dI_s}{dz} = I_s \sigma_s (N_2 - N_0) \tag{5.3}$$

where in the above N_i depends the position inside the crystal z.

Transitions from spontaneous emission happen much less frequently than transitions from stimulated emission. To quantify this statement consider the intensity of the focused pickup radiation in the amplifier. The radiated energy in the fundamental is on the order of 50 meV which (as we will later see) will be focused to spot radius of approximately 100 μm. If the beam has 10^7 electrons then, accounting that the repetition rate in IOTA is 7.5 MHz, this gives an average signal intensity of $I_{so} = 0.6$ mW/cm^2. From the second formula in Eq. 5.1 the transition rate is given as $\sigma_s I_s / h\nu_s$ this value should be compared to the rate of

spontaneous emission $1/\tau_2$ where $\tau_2 = 5.5\ \mu$s [36] giving a ratio of transition rates (stimulated to spontaneous) of $\approx 10^{-7}$. We can therefore neglect I_s in the above rate equations and consequently (assuming CW laser pumping) look for a steady state solution of system in Eq. 5.1.

The decay time of 3 and 1 is much shorter than 2 so we can say $N_3 \ll N_0$ and $N_1 \ll N_2$. Then from the first equation in Eqs. 5.1 we get

$$N_3 \approx \frac{I_p \sigma_{pa} N_0}{h\nu_p \kappa_3}. \tag{5.4}$$

From this expression we can eliminate N_3 from the second formula of Eq. 5.1 and using Eq.'s 5.2 and 5.3 we obtain an expression relating the pump attenuation to the signal gain

$$\frac{dI_s}{dz} = -\frac{\sigma_s \tau_2}{h\nu_p}\frac{dI_p}{dz}, \tag{5.5}$$

then by defining $G \equiv I_s/I_{so}$ it is straightforward to show that

$$G = \exp\left(\Delta I_p \frac{\sigma_s \tau_2}{h\nu_p}\right), \tag{5.6}$$

where $\Delta I_p = I_P(z=0) - I_p(z=L)$ is defined so that it will be positive and L is the length of the crystal.

Thus all that remains to find the gain is the pump attenuation through the crystal. Typically light decays exponentially through a material with an attenuation constant $\alpha = N_T \sigma_{pa}$ where $N_t \approx N_0$ is the total ion doping concentration see Table 5.1. Considering the case of Cr:ZnSe with the pump intensities needed for the desired gain, the ground state starts to deplete such

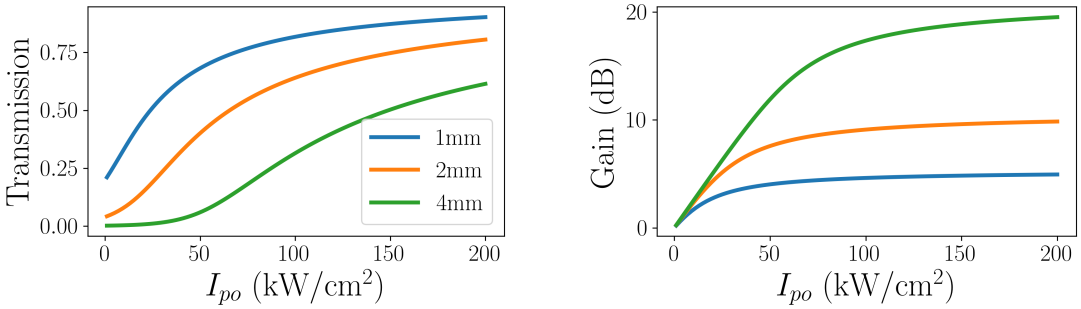

Figure 5.2: The transmission and Gain curves for a single-pass through a Cr:ZnSe amplifier as a function of incident pump laser intensity for 3 different crystal lengths. Transmission is for 1908 nm light and amplification is at 2.45 μm.

that $N_T \approx N_0 + N_2$ and the crystal exhibits an intensity-dependent transmission. Returning back once more to the second equation of Eq. 5.1, eliminating N_2 and solving for N_0 yields

$$N_0 = N_T \frac{1 + I_p \frac{\sigma_{pe}\tau_2}{h\nu_p}}{I_p \frac{\tau_2}{h\nu_p}(\sigma_{pa} + 2\sigma_{pe})}, \tag{5.7}$$

which can be plugged into Eq. 5.2 finally resulting in

$$\frac{dI_p}{dz} = -I_p N_t \left(\frac{\left(1 + I_p \frac{\sigma_{pe}\tau_2}{h\nu_p}\right)(\sigma_{pa} + 2\sigma_{pe})}{I_p \frac{\tau_2}{h\nu_p}(\sigma_{pa} + 2\sigma_{pe})} - \sigma_{pe} \right). \tag{5.8}$$

Numerical integration of the above equation can be used to find the change in pump intensity ΔI_p over the crystal length and thus infer the gain. For many amplifying mediums $\sigma_{pe} = 0$ and Eq. 5.8 can be solved in terms of the transcendental Lambert-W function; see Appendix C for details.

The gain and transmission for a single-pass through a Cr:ZnSe amplifier is shown in Fig. 5.2. The curve for the 1 mm crystal corresponds to 1.45 mm of optical delay and is the expected length to be used for the active OSC in IOTA. The transmission is seen to increase rapidly with higher pump intensities. This implies a leveling off of the absorbed pump intensity ΔI_p

and consequently limits the gain. At 125 kW/cm^2 the gain is 7 dB and can not increase further. For crystals with longer length the onset of the increased transmission is delayed and the corresponding gain is significantly increased. Unfortunately a longer crystal can not be used in the IOTA experiment given the limited optical delay set by the particle delay in the chicane bypass.

5.1.1 Pulse amplification OSC

The formulas developed in the previous section apply to a plane-wave which, as we have already investigated Chapter 4 is not the case for the pulsed pickup radiation to be amplified. The propagation of a pulse through an amplifier is best understood in the Fourier-plane where the electric field harmonic is modified as

$$E_2(\omega, z) = E_1(\omega)\left[iz\beta\left(1 + \frac{\chi'}{2}\right) + z\frac{\beta\chi''}{2}\right] \tag{5.9}$$

where $E_1(\omega)$ is the original field, $\beta \equiv \omega c/n$ with n the index of refraction as before, χ' and χ'' are the real and imaginary parts of the atomic line shape i.e. $\chi_{at} \equiv \chi'(\omega, z) + i\chi''(\omega, z)$ is the complex Lorentzian atomic line shape given as [38]

$$\chi_{at} = -\chi_0''\left[\frac{\Delta x}{1 + \Delta x^2} + i\frac{1}{1 + \Delta x^2}\right], \tag{5.10}$$

where $\Delta x \equiv 2\frac{\omega - \omega_a}{\Delta\omega_a}$ with ω_a being the mid-band angular frequency and $\Delta\omega_a$ is the FWHM amplifier bandwidth. The amplitude is

$$\chi_o'' = \frac{3}{4\pi^2}\frac{\Delta N(z)\lambda^3}{\Delta\omega_a \tau_2 n^3}, \tag{5.11}$$

and mid-band values for λ and n of the amplifier are used in its evaluation. In the latter equation $\Delta N(z) = N_2(z) - N_1(z)$.

The argument in the exponent of Eq. 5.9 is complex. The real part is responsible for the amplitude growth (gain) of the signal. The imaginary part results in a (wavelength dependent) phase shift. Going further the imaginary part has two terms. The first term $z\beta$ is related to phase-shifts arising from propagation through the host medium (this includes e.g. group velocity dispersion effects, in the case of Cr:ZnSe the host is ZnSe).

The other imaginary term of the exponent results in a distortion of the pulse related to the finite bandwidth of the amplifier. Its contribution is found by integrating over the crystal length. In Eq. 5.10 $\Delta N = N_2 - N_1 \approx N_2$ which is related to the signal intensity as $N_2 = \frac{1}{\sigma_s I}\frac{dI_s}{dz}$. Then noting that $\sigma_s \approx \frac{3}{2\pi}\frac{\lambda^2}{\tau_2 \Delta\omega_a n^2}$ we get

$$\Phi_{amp} = \frac{\beta}{2}\int \chi'(\omega, z)dz = -\frac{1}{2}\frac{\Delta x}{(1+\Delta x^2)}\int \frac{1}{I_s}\frac{dI_s}{dz}dz = -\frac{1}{2}\frac{\Delta x}{(1+\Delta x^2)}\ln(G). \tag{5.12}$$

In section 5.3 Φ_{amp} is measured in the case of a Ti:Sapphire amplifier. A similar integration over χ'' is performed for the amplitude growth and we arrive at a formula giving the modification of a small-signal electric field of arbitrary wavelength dependence through the amplifier

$$E_2(\omega, z) = E_1(\omega)\exp[i(z\beta + \Phi_{amp})]G^{\frac{1}{2(1+\Delta x^2)}}. \tag{5.13}$$

Note that in the above equation in the limit that $\Delta x \to \infty$ it returns

$$E_2(\omega, z) = E_1(\omega)\exp(iz\beta)\sqrt{G} \tag{5.14}$$

which describes a pulse passing through a dispersive medium with its field amplitude increased by $\sqrt{G}$ as would be expected.

5.2 Active OSC in IOTA

The simulation methods developed in Chapter 4 using SRW can be extended to include an optical amplifier and addresses two separate topics: (i) The transport optics are constrained to have a matrix $\pm\mathbf{I}$ which will determine the spot radius of the pickup radiation in the amplifier. This in turn determines the required pump laser power. (ii) In a single-element host dispersion and amplifier bandwidth is included providing a realistic model of the amplified pulse and increased kick amplitude. Just like in the case of including chromatic effects, this is straightforward to implement in SRW since computations are done in the Fourier-domain.

5.2.1 Pickup spot radius in the amplifier

The laser pump intensity determines the gain which for the foreseen 7 dB of amplification would need to be 125 kW/cm^2. To keep the laser power reasonable we would like the spot radius to be $\rho_p \approx 100$ μm so that total power is around 40 W. In order to choose between the positive or negative telescope we compute the transfer matrix from pickup center, $\boldsymbol{x}_m = (x_m, \theta_m)$ to chicane center $\boldsymbol{x}_m = (x_f, \theta_f)$ (where the amplifier is located)

$$\boldsymbol{M} = \begin{bmatrix} 1 & L_2 \\ 0 & 1 \end{bmatrix} \begin{bmatrix} 1 & 0 \\ \frac{-1}{F} & 1 \end{bmatrix} \begin{bmatrix} 1 & L_1 \\ 0 & 1 \end{bmatrix} = \begin{bmatrix} 1 - L_2/F_1 & L_1 + L_2 - L_1 L_2/F_1 \\ -1/F_1 & 1 - L_1/F_1 \end{bmatrix} \tag{5.15}$$

and it should be noted that M is valid for both transverse planes (x, x') and (y, y') owing to the cylindrical symmetry of the transport system and assumed symmetry of the radiation field.

Once again consider a ray originating from the pickup center on axis with an angle θ_m so

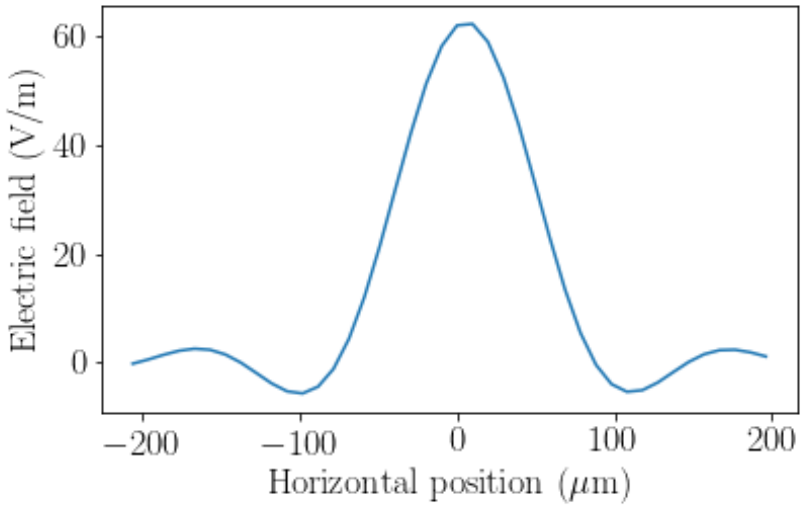

Figure 5.3: $E_x(x)$ in the plane of the amplifier.

the ray arrives at an amplifier with a horizontal coordinate $x_f = \theta_m M_{12}$.

Referring to Eqs. 3.24 and 3.25 we get that for the -**I** telescope, $x_f = L_2\theta_m$. Given that $\theta_m \approx$ 4.1 mrad L_2 would need to be made as short as 2.4 cm. This in turn determines $F_1 = 2.4$ cm which is already a strong lens; but even worse it determines $F_2 = -410$ μm which is an impractically small focal length. The +**I** telescope on the other hand results in $x_f = 0$ and so looks like a better choice. It should be noted that this estimate neglects diffraction of the pickup radiation and the length over which the radiation was emitted.

To confirm that a +**I** telescope is suitable the horizontal dependence of the electric field was computed with SRW (in the time domain) in the plane of the amplifier and is shown in Fig. 5.3. Using the telescope values presented in Table 5.2 we see the desired ρ_p is achieved.

Because the pump and signal photon energies are different then by consideration of energy conservation a fraction of the laser pump power is transformed into heat as

$$P_h = \Delta I_p (1 - \frac{\lambda_p}{\lambda_s}) \pi \rho_p^2. \tag{5.16}$$

If the pump laser is assumed to be a flat-top distribution in the radial direction then there is a temperature dependence given by:

$$T(\rho) = \begin{cases} \frac{P_h}{4KL\pi\rho_b^2}(\rho_p^2 - \rho^2) + T(\rho_p) & \rho < \rho_p \\ \frac{P_h}{2KL}\ln(\frac{\rho_{xtal}}{\rho}) + T(\rho_{xtal}) & \rho > \rho_p \end{cases} \tag{5.17}$$

where ρ_{xtal} is the radius of the crystal assumed to be cylindrical in shape. The surface

symbol	value	units
L_1	154	cm
L_2	21	cm
F_1	18.5	cm
F_2	1.3	cm
$\gamma\theta_m$	0.8	-
Outside lens radius	6.3	mm

Table 5.2: Geometrical parameters of lens telescope for active test of the OSC in IOTA.

where the heat exchange occurs is assumed to be the lateral surface of the cylindrical crystal of length 1-mm and a 5-mm radius. K is the crystal's thermal conductivity. $T(\rho_{xtal})$ is the temperature at the crystals surface and is equal to the cooling fluid. Assuming liquid nitrogen cooling so that $K = 1.0$ W/m-K the total temperature change from crystal center to surface is 15 K.

The signal radiation is focused inside of ρ_p where there is a parabolic temperature dependence. The index of refraction of the host medium is temperature dependent. For small variations in temperature, the change in n goes as $\Delta n(T) = \frac{dn}{dT}T$ implying it too will have a parabolic dependence in the radial position and thus acts like a lens with a focal length given by [32]

$$f_{th} = \frac{K\pi\rho_p^2}{2P_h}\frac{dn}{dT}. \tag{5.18}$$

Therefore the pumping intensity uniquely determines both the gain and thermal lensing focal length. For the 7 dB amplifier expected to be used in IOTA $f_{th} = 5$ cm which does not match F_2 in Table 5.2. Therefore additional focusing power is required. This can be accomplished by curving the surface of the crystal or including an additional lens near the amplifier.

5.2.2 Pulse amplification with SRW

Using SRW both the host dispersion and the amplifier bandwidth are included in computing the amplification of the pickup radiation. For host dispersion the Sellmieir formula with coefficients for ZnSe was used [31]. For the amplifier bandwidth the cross-section used in computing the gain was modeled as the sum of two Gaussian distributions centered at 2.07 and 2.45 μm and the gain was set to be 7 dB at 2.45 μm. The cross-section is plotted in Fig. 5.4.

In the right pane of Fig. 5.4 the undulator wave-packet in the kicker center is plotted exhibiting these various effects. The original, unamplified pulse, is plotted in red and for an ideal amplifier (no dispersion and infinite bandwidth) its amplitude would increase by ≈ 2.2 (corresponding to 7 dB of gain). In green the amplifier bandwidth is accounted and the amplitude is reduced by 14 % of the ideal amplifier. Including host dispersion results in a further reduction of 12 %. Computing the kick with the methods presented in Chapter 4 results an increased kick amplitude of 1.8 over the passive OSC.

5.3 Ti:Sapphire amplifier and Φ_{amp}

Although the active OSC in IOTA will be based on Cr:ZnSe, Ti:Sapphire which lases at a smaller central wavelength of 780 nm is still an important amplifier to be considered

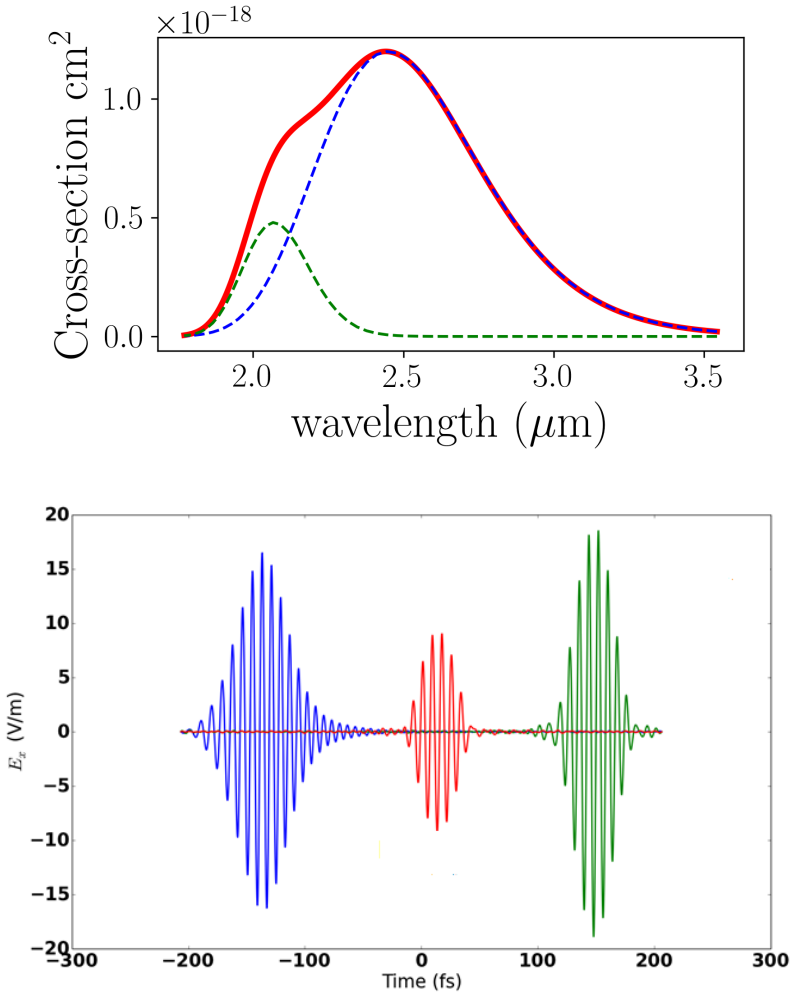

Figure 5.4: Left: The modeled cross-section for Cr:ZnSe used for gain calculations (red solid line) with the individual Gaussian distributions comprising it (blue and green dashed lines). Right: The pulse in the kicker center with the amplifier off (red), the pulse with the amplifier on but not including host dispersion (green) and the pulse with the amplifier on and including host dispersion (blue).

for future experiments with the OSC [37]. In addition at an earlier stage of our work we considered Ti:Sp as a possible candidate gain medium for the IOTA experiment.

Some important parameters of Ti:Sapphire are given in Table 5.3. In this section we describe an attempt to measure Φ_{amp} from Section 5.1.1 [39]. This was done by inserting a 2-mm thick Ti:Sapphire crystal with an absorption constant $\alpha = N_T\sigma_s = 10$ cm^{-1} into one

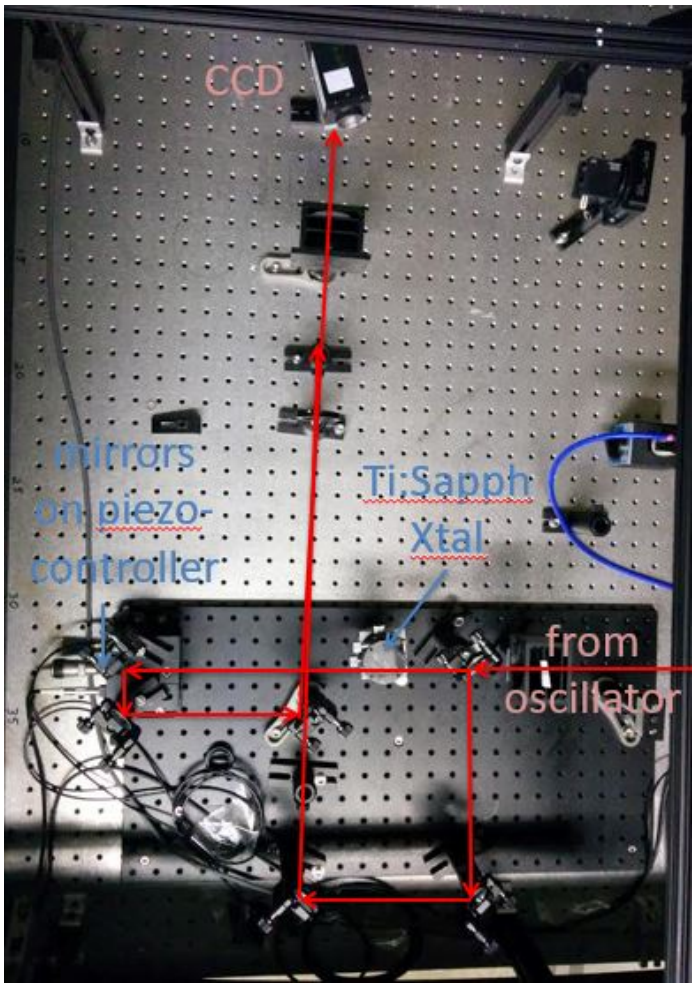

Figure 5.5: The Mach-Zhender interferometer used in the experiment to measure Φ_{amp}.

leg of a Mach-Zhender interferometer (see Fig. 5.5). A interference pattern was obtained immediately before and during amplification. A shift in pattern corresponded to a change in the amplified radiation's phase.

As a seed a Spectra-Physics Tsunami Ti:Sapphire laser which can operate either CW or mode-locked (pulsed). Because we were interested in measuring $\Phi_{amp}(\lambda)$ the measurements were done in CW operation thereby reducing the bandwidth of the laser to a fraction of a nm so that the signal wavelength is well defined; but in order to equalize the path lengths and do gain measurements (from a photo-diode) the seed laser was mode-locked while obtaining

Parameter	Value	Unit
Florescence peak	780 [40]	nm
Absorption peak	500 [40]	nm
$\Delta\omega_a/2\pi$	95 [40]	THz
τ_2	3.2 [32]	μs

Table 5.3: Parameters for Ti:Sapphire gain medium.

the interference pattern. The phase shift was measured from 740-810 nm and the wavelength was calibrated with an Ocean-Optics fiber spectrometer.

The pump laser was a Spectral-Physics Quanta Ray centered at 532nm. The pump pulse energy was 65 mJ and operated 10 Hz frequency. The pump path was counter to the signal with a small $\approx 10\,\text{deg}$ angle so that a beam-dump could be inserted before the pump encountered any of the optics of the interferometer. For these pump parameters, $G \approx 3$ was typically observed.

To record the interference pattern a Dicam-Pro intensifier camera with a 'double-shutter' mode which allowed two images to be taken within 2 μs of each other (see images in Fig. 5.6). A beam-splitter placed in front of the camera was used to split the light so that the signal could be simultaneously seen on a photo-diode and the camera.

Triggering was done off the Q-switch signal of the pump and a delay unit was used to adjust the timing so that the first image took place ≈ 1.5 μs before amplification and the 2nd was done 0.5 μs after (see Fig. 5.6). Because the pump laser is pulsed the amplification is transient and therefore a relatively short exposure time of 40 ns was used. At each wavelength 20 sets of interference patterns were taken. For each set a projection along the x-axis was made and the shift in the fringe pattern was recorded and converted to degrees (plot (b) in Fig. 5.6). In addition to a phase shift from Φ_{amp} a non-resonant (wavelength independent) index of refraction was report in [41]. To compensate for this a constant is added so that $\Phi_{amp}(\omega_a) = 0$.

In Fig. 5.6 Φ_{amp} computed from Eq. 5.12 (solid green line) is plotted along with the mea-

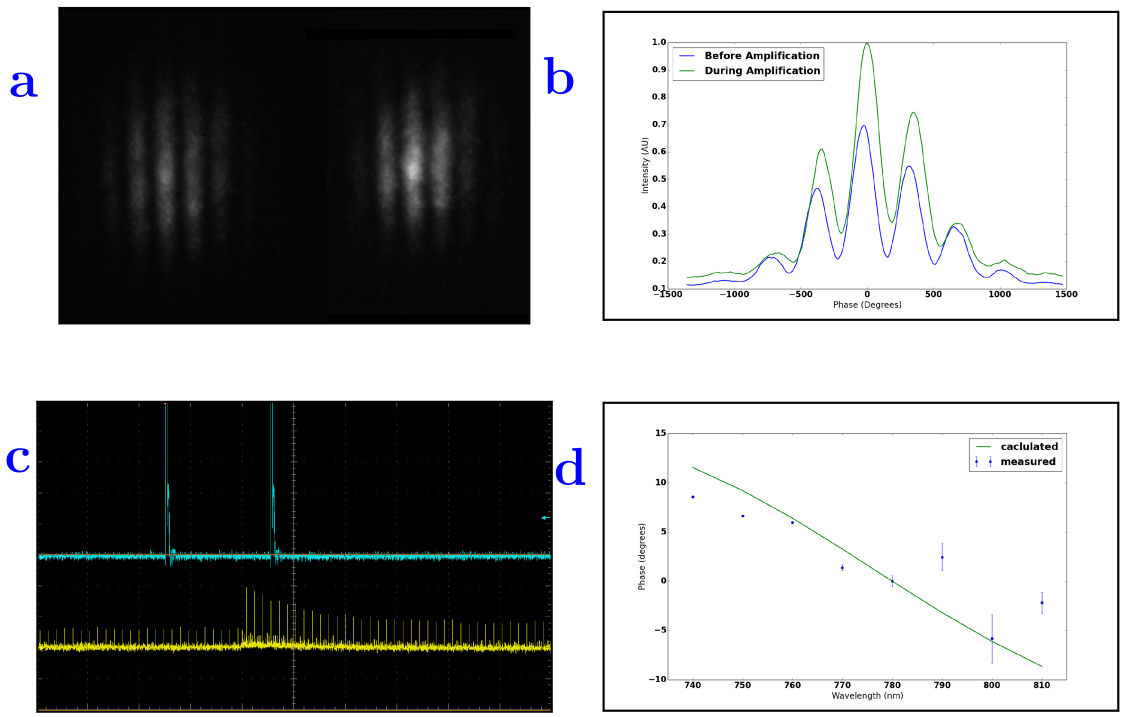

Figure 5.6: (a) Interference patterns from before and during amplification and (b) there projections along the x-axis. (c) a traces from the oscilloscope used for the timing of the camera. The blue traces indicate when an image was taken. The yellow trace shows pulses from the seed laser with amplification visible. (d) Computed and measured ϕ_{amp}

surement (blue dots) in rough agreement. The technique presented here can be adapted and refined to the case of Cr:ZnSe in the near future.

CHAPTER 6

DIAGNOSTIC FOR PATH EQUALIZATION BETWEEN THE REFERENCE PARTICLE AND PICKUP WAVE-PACKET

In this brief chapter we propose a method for setting the arrival time between the reference particle and pickup radiation at the entrance of the kicker [42]. Such a diagnostic is critical to the success of the proposed experiment at IOTA. We especially explore its experimental implementation and show the signal associated to the diagnostic to be stronger than the background synchrotron radiation collected in the diagnostic system.

6.1 Method for path equalization

Seemingly one of the biggest obstacles in the implementation of the OSC is the timing of the arrival of the particle with its radiation wave-packet. In fact we are supposing not just that we can time the arrival of the particle so that it overlaps with its own wave-packet; for the cooling to be near optimal this timing must be done to a small fraction of the radiation wavelength, implying sub-femtosecond accuracy. Fortunately, the timing can be inferred from the downstream intensity of the summed radiation emitted from the pickup and kicker. Let's consider case of passive OSC at 2.2 μm. Take an arbitrary particle (labeled n) with the arrival phase at the kicker given by $\Psi_n = \psi_{te} + \psi_n$ where $\psi_{te} = ks_d$ is the error in phase that results from error in the particle path length[1] and $\psi_n = a_x \cos(\psi_x) + a_u \sin(\psi_u)$ where a_x and a_u are defined in Eqs. 2.27 and 2.37. In the latter equation ψ_x and ψ_u are the particles

[1] That is a mis-match in the delay of the pickup radiation propagating through the transport line and the path length created from the chicane dipoles. This error is the same for all particles.

synchrotron and betatron phase. For simplicity we will assume the undulator wave-packet has a uniform envelope with length $L_w = N_u\lambda_o$. The energy loss of the particle is

$$\Delta\mathcal{E}_n = -\Delta\mathcal{E}_{tot}\left(1 + F_h(K,\gamma\theta_m)\sin(\Psi_n)\frac{L_w - |s_d| - s_n}{L_w}\right) \tag{6.1}$$

where $\Delta\mathcal{E}_{tot}$ is the total energy radiated in both kicker and pickup in the absence of OSC, $F_h(K,\gamma\theta) \leq 1$ is defined in Eq. 3.22 and $s_n = \psi_n/k_o$ is the longitudinal displacement of the particle relative to the reference particle. We therefore see the energy loss of the particle going through the insertion is modulated sinusoidally with respect to its deviation, but also additionally with respect to the timing error [43]. There would then be a modulation in the summed pickup and kicker radiation (in the first harmonic) observed downstream of the kicker that correlates to the timing error.

Now consider the combined energy modulation of all particles in the beam. If we assume a Gaussian distribution for the beam in the longitudinal and horizontal planes then the standard deviation of particle's longitudinal displacement is $\sigma_s^2 = (s_u\sigma_u)^2 + s_x\epsilon_o$ and the total radiated energy leaving the kicker is

$$\Delta\mathcal{E}_{beam} = N\Delta\mathcal{E}_{tot}\left(1 + \int \frac{F_h(K,\gamma\theta_m)}{\sigma_s\sqrt{2\pi}}\frac{L_w - |s_d| - s}{L_w}\cos\left(k_o(s+s_d)\right)\exp\left(\frac{-s^2}{2\sigma_s^2}\right)ds\right) \tag{6.2}$$

where $s_x = 3.5$ μm is inferred in Eq. 2.37 and $s_u = (M_{51}D + M_{52}D' + M_{56})$ =1.7 mm. The integral can be evaluated by replacing the cosine term with a complex exponential and taking the real part after integration. Using the following two integral identities

$$\int \exp(-x^2)dx = \sqrt{\pi} \quad \text{and} \quad \int x\exp(-x^2)dx = 0 \tag{6.3}$$

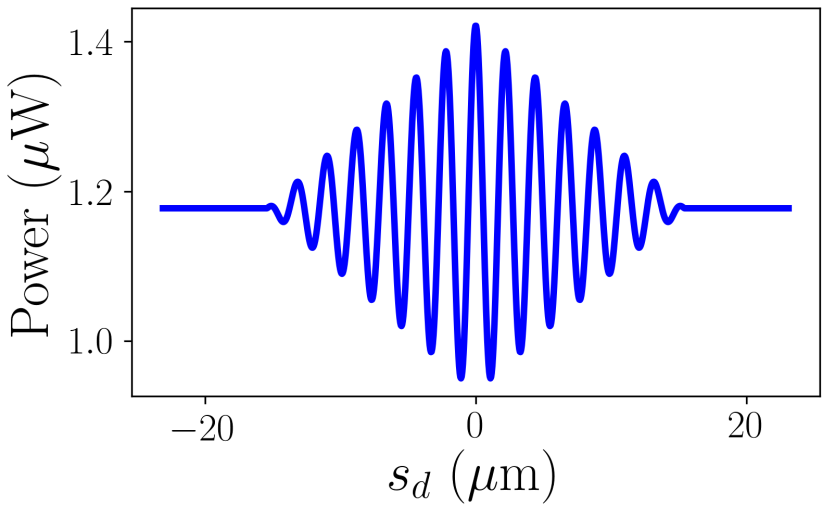

Figure 6.1: The emitted power from the combined pickup and kicker radiation while scanning through particle arrival time.

we arrive at the result

$$\Delta\mathcal{E}_{beam} = N\Delta\mathcal{E}_{tot}\left(1 + \frac{L_w - |s_d|}{L_w}\cos(k_o s_d)\exp\left(\frac{-k_o^2\sigma_s^2}{2}\right)F_h(K,\gamma\theta_m)\right) \tag{6.4}$$

The above expression can be converted to average power by multiplying by the revolution frequency in IOTA and is plotted in Fig. 6.1. The relative amplitude of the intensity modulation is $F_h(K,\gamma\theta_m)\exp\left(\frac{-k_o^2\sigma_s^2}{2}\right)$ which for 2.2 μm OSC has a value of 0.21. The intensity modulation with respect to timing error should then be quite visible. This is a consequence of the moderate K value and large cooling ranges in the experiment design.

If $\cos(\psi_{te}) > 0$ a timing error results in the reference particle receiving a kick and there is thus a small change in the energy loss around the ring. This change in energy loss is automatically compensated by a change in the RF phase of the reference particle and particles damp around this new point. When $\cos(\psi_{te}) < 0$ particles in the cooling range are excited to $[a_x, a_s] = [\mu_{1,1}, 0]$ or $[0, \mu_{1,1}]$ (see Appendix B). Therefore during longitudinal overlap pro-

cedure a scan of s_d should be done on a time scale shorter than the damping time to prevent beam loss. In principle there are two ways to scan s_d. The first method would be varying the current in the chicane dipoles and thus changing the reference particle's path length. This approach has been ruled out since it results in the reference particle having a horizontal displacement in the chicane sextupoles [2]. The second way to scan s_d is by creating a variable optical delay in the optical transport. This can be achieved, e.g., by placing a glass slab in the optics transport. The tilt of the glass determines the path length thickness (and thus arrival time). Using a pair of slabs allows for the angles to be selected to set the delay while also enabling a correction to the transverse displacement arising from the wave-packet passing through the glass. Note that coherent interference between undulator radiation has already been observed [44].

Finally, we should point out that the third-harmomnic radiation would be more convenient to implement the proposed diagnostics (given the wide range of detectors available in the optical regime). Unfortunately, the harmonics are temporally separated due to second order dispersive effects in the transport line and therefore does not interfere with its parent particle in the kicker. Nevertheless, the third-harmonic radiation will be useful in ensuring transverse overlap between pickup and kicker fields.

6.1.1 Practical implementation in the IOTA ring

One of the main challenges in implementing the proposed temporal-overlap technique in IOTA comes from the need to detect the radiation downstream of a 30-deg dipole bending magnet; see Fig. 6.2 Therefore the proposed diagnostic signal will be overlapping with the radiation emitted in the dipole magnet. To check the relative intensities the radiation from

[2] two sets of sextupoles sit between the outer dipoles of the chicane.

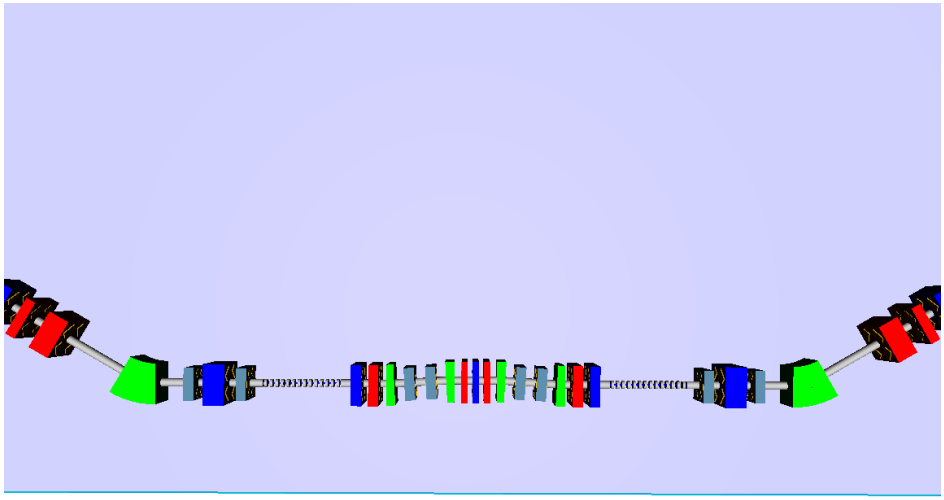

Figure 6.2: The OSC chicane. The diagnostic station will be located just past the 30-deg downstream bending magnet (left-most green element, the electron beam and radiation move from right to left in the diagram.) where radiation from both undulators and the bending magnet overlap spatially.

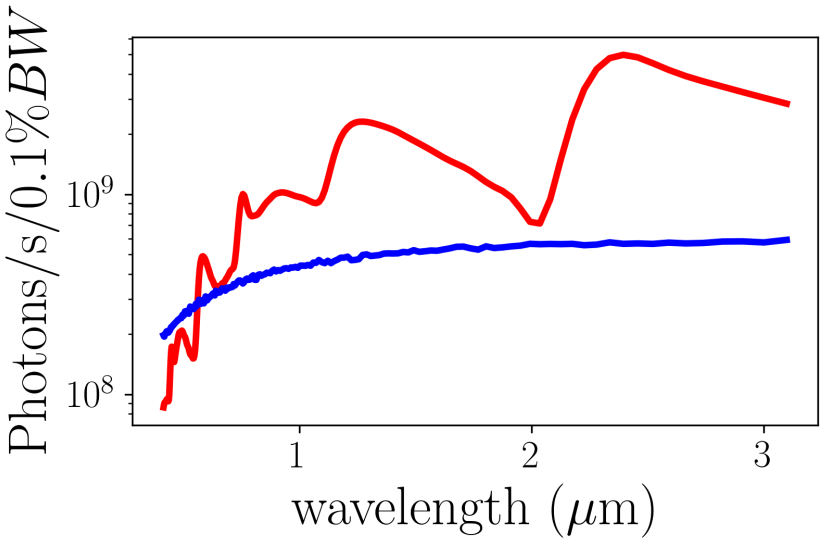

Figure 6.3: Integrated kicker (red) and dipole radiation (blue) downstream of the OSC insertion.

the kicker (no pickup signal or interference) is plotted against the dipole radiation as shown in Fig. 6.3 revealing bending radiation should not effect the diagnostics. Spatial integration of the intensities was done over a 6 mrad circular aperture and the relative placement of kicker and bending magnet is accounted. The latter figure indicates that the kicker radiation intensity is, when averaged over the fundamental band of the OSC, 6.8 times brighter than the background synchrotron radiation thereby giving confidence on the viability of the proposed method.

CHAPTER 7

SIMULATIONS OF OPTICAL STOCHASTIC COOLING WITH ELEGANT

In this chapter we present simulations of the OSC in IOTA using the particle tracking code ELEGANT [45]. To model the OSC, the particle time-of-flight from pickup to kicker entrances was recorded and used to make a corresponding energy kick. Good agreement is observed between the simulated damping rates to those derived in Chapter 2. We then go on to consider how damping rates are modified when there is transverse separation between the pickup radiation and particle in the kicker and confirm the necessity of sextupoles for non-linear path lengthening correction.

7.1 Introduction to ELEGANT

ELEGANT stands for "ELEctron Generation ANd Tracking" and is a program with 6D particle tracking capability in an accelerator and even more advanced things like lattice optimization for betatron functions, tunes and emittance. ELEGANT has built in elements of most accelerator components (e.g. dipoles, quadrupoles, undulators etc..) which can be implemented either through a matrix formulation (of selectable order), a canonical kick or numerically integrated element.

Inputs and outputs follow a 'self describing data set' (SDDS) which allows users to prepare and process scripts in an automated way. This is also convenient for performing multi-stage simulations.

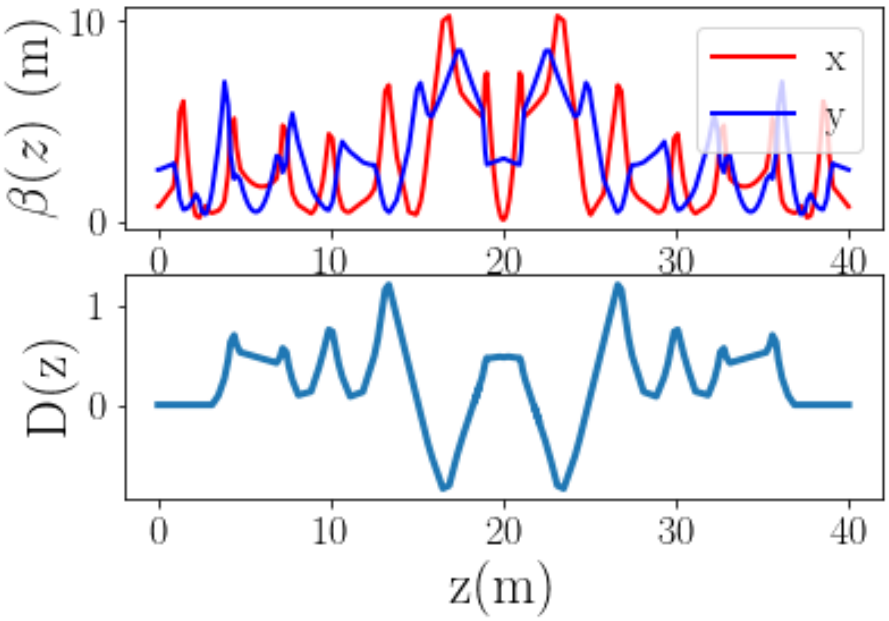

Figure 7.1: The vertical and horizontal beta functions computed with ELEGANT (top) and the horizontal dispersion function (bottom). The chicane center corresponds to $z = 20$ m.

7.2 Implementation of IOTA-OSC lattice in ELEGANT

The previously [46] designed lattice was built by first considering the requirements of the lattice functions at the chicane center (e.g. small β^* and a large dispersion invariant) and then building around the rest of the ring. Although a large dispersion invariant in the chicane center is beneficial to the horizontal cooling range, outside of the ring it is minimized in order to achieve as small an equilibrium beam emittance as possible.

As a first step of our OSC simulations we implemented the IOTA-OSC ring in ELEGANT. The vertical and horizontal beta-functions are plotted in Fig. 7.1.

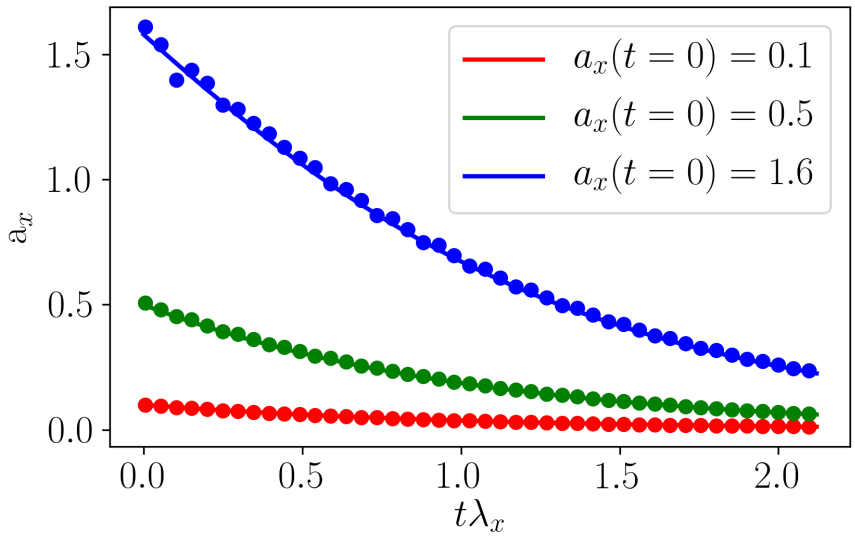

Figure 7.2: The amplitude of longitudinal displacement $a_x(t)$ for different initial amplitudes. Circles are computed from ELEGANT outputs while solid lines are from numeric integration of Eq. 7.1.

7.3 Simulation of OSC horizontal damping rate

In ELEGANT the kick is computed by recording the arrival times of the particle in the pickup and kicker, t_p and t_k respectively. During the first pass through the insertion the average time difference $\langle t_k - t_p \rangle$ of the bunch is computed and used to compute the arrival phase of the reference particle. In subsequent passes through the cooling insertion a particles time of flight $t_k - t_p$ is used to find s_n and compute the corresponding change in the particles momentum. a_x was computed with Eq. 2.37 using M_{51} and M_{52} from Table 2.1 and the ELEGANT generated Twiss parameters α and β taken at the pickup center.

Recall that cooling rates are coupled between longitudinal and horizontal planes; therefore to observe horizontal cooling the longitudinal emittance was set to zero. In this case the damping rate should go as; see Eq. 2.39

$$\frac{da_x}{dt} = -2J_1(a_x)\lambda_x. \tag{7.1}$$

Figure 7.2 compares the evolution of a_x obtained from numerical integrations of Eq. 7.1 against results inferred from tracking simulations with ELEGANT given three different initial conditions for $a_x(t = 0)$. In ELEGANT the particles initial Courant-Snyder invariant, ϵ, is set which has the form

$$\epsilon = \beta x'^2 + 2\alpha x x' + \gamma x^2. \tag{7.2}$$

At each turn the particles x and x' coordinates are recorded and used to recompute ϵ which can then be used to compute a_x with the aid of Eq. 2.37.

Our model neglects kicks by neighboring particles since we are interested in the dynamics of a single classical particle in the accelerator. This choice is further justified considering that the OSC test in IOTA will first be done passively and later using a low-gain amplifier where the kick amplitude is far from the optimal gain. Consequently the incoherent kicks from neighboring particles is negligible.

We can account for the horizontal separation between the radiation and particle in the pickup that results from a non-zero horizontal position of the particle when entering the pickup. This is particularly important in active OSC. In Section 5.2.1 we introduced an optical system consisting of a telescope with a transfer matrix $\pm\mathbf{I}$ where $\mathbf{I}$ is the identity matrix is needed in order to keep the pump laser power reasonable. For the $+\mathbf{I}$ telescope if a particle radiates at position x_p in the pickup its imaged radiation will appear at x_p in the kicker. However the beam optics have negative diagonal elements in the horizontal plane. For instance considering the beam optics transfer matrix as $-\mathbf{I}$ means that the separation between the particle and light is $\Delta x_l = 2x_p$. At the pickup center $\beta_x = 5.7$ m and so a particle with its Courant-Synder invariant equal to the beam emittance will be displaced (at its maximum displacement in x over the course of its betatron oscillation) 240 μm. Using

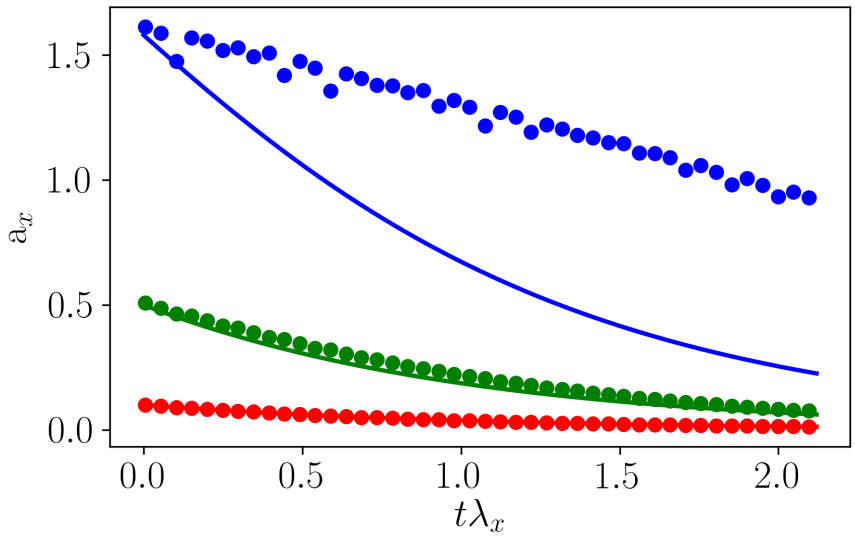

Figure 7.3: OSC damping rates accounting separation of light and particle when a +**I** telescope is used for the optical transport. The same initial conditions as used in Fig. 7.2 are considered here.

Eq. 3.17 the undulator radiation spot size (from center to zero field crossing) in the kicker is 590 μm resulting in an 30% reduction in the field amplitude. Figure. 7.3 shows the damping $a_x(t)$ assuming a +**I** telescope. The particles coordinates in pickup and kicker locations from ELEGANT were used directly to compute its separation from the field. As expected particles with large amplitudes are affected most with a significant decrease in the damping rate.

7.4 Non-linear path lengthening corrections

From Eq. 2.41 the horizontal emittance is seen to increase with decreasing β^* and is therefore made small in the chicane center. However a small value of β^* implies a large angle

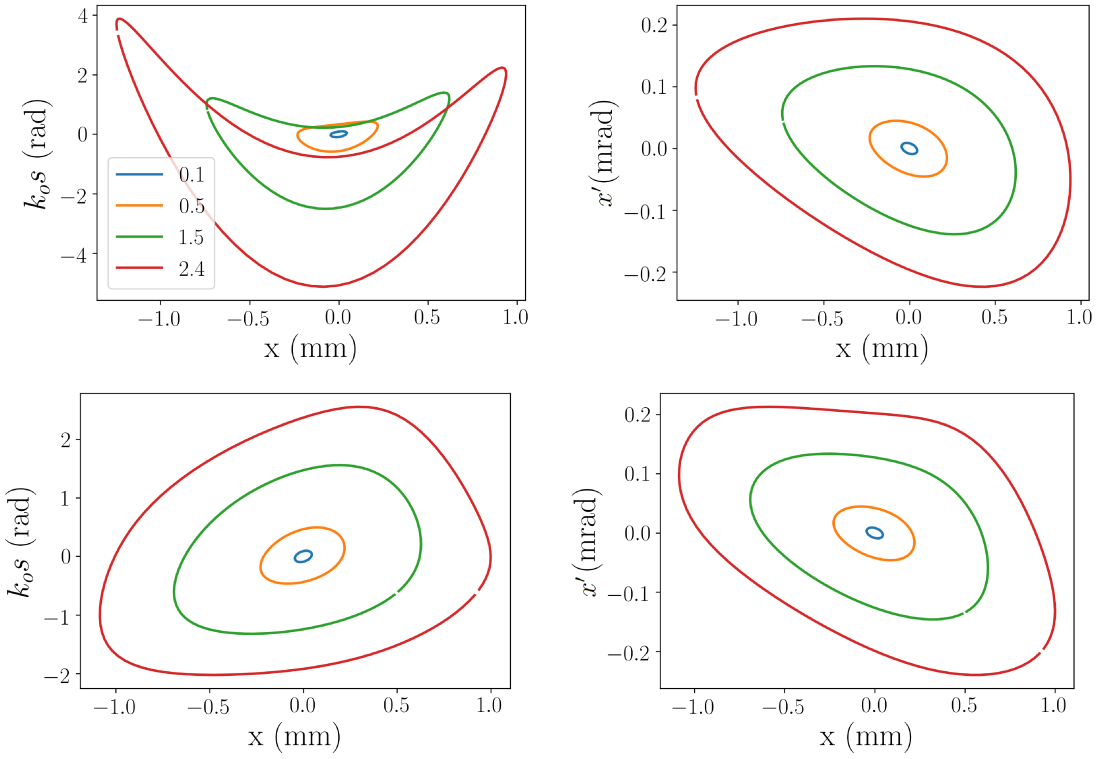

Figure 7.4: Contours in the $x-k_o s$ and $x-x'$ space for different values of a_x of 0.1 (turquoise), 0.5 (orange), 1.5 (green) and 2.4 (red). The top row is without the sextupoles to correct the path lengthening and the bottom row includes them.

in the particle's trajectory. This results in a 2nd order, non-linear path lengthening effect which was previously estimated as [21]

$$\Delta s_2 = \frac{1}{2}\int \left(x'(z)^2 + y'(z)^2\right) dz. \tag{7.3}$$

The nonlinear path lengthening results in a distortion of the x- $k_o s$ space that is an ellipse in the absence such lengthening. Two sets of sextupoles placed between the outer chicane dipoles are used to correct the path lengthening. Since our ELEGANT simulations already compute the particle time-of-flight it is straightforward to check this result as shown in

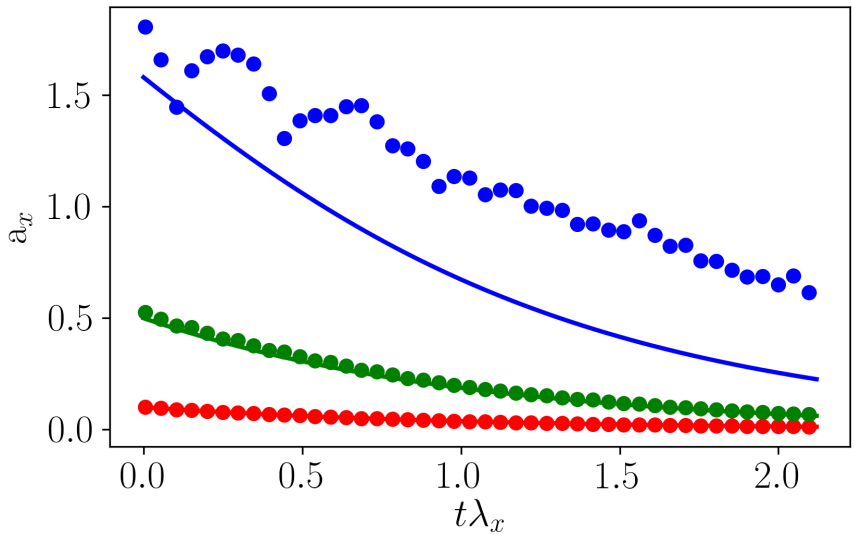

Figure 7.5: OSC damping rates without correction of the non-linear path lengthening.

Fig. 7.4. Note also that the inclusion of the sextupoles results in a minor distortion of the x, x' ellipse.

Going further we can compute the horizontal damping rate in the absence of sextupole corrections as shown in Fig. 7.5. Comparing the latter figure with Fig. 7.2 (where the sextupole magnets were set to their nominal value), we see that only large-amplitude particles are affected as the associated amplitude decay gets weaker and is further away from the theoretical prediction obtained via numerical integration of Eq. 7.1.

CHAPTER 8

CONCLUSION

The work presented in this thesis describes the light transport and amplification of pickup radiation into the kicker as well as the subsequent energy exchange between the particle and radiation field. This was done by first applying the Lienard-Wiechert potentials to a particle passing through an undulator and then using Fourier-optics based transformations to obtain the focused field in the kicker. From this we were able to get formulas which are useful in determining the properties of the pickup and kicker undulators and also the optics of the transport line. The model was then refined and wave-optics simulations were performed to verify the theoretical formulas obtained. The numerical simulations also provided a tool to go beyond the simplified theoretical model and include realistic effects to finally accurately compute the energy exchange in the kicker between a particle and its own radiation field (emitted in the pickup).

We then expanded our study to design an optical amplifier that would be needed for OSC in a collider. We especially developed expressions describing the gain from a single-pass amplifier based on a laser pumped solid-state gain medium. Since the active test of the OSC at Fermilab called for amplification of light in the mid-IR region, these expressions were applied to Cr:ZnSe, the lasing medium we identified as the best candidate for active OSC in IOTA. Our investigation of Cr:ZnSe as a lasing medium revealed a severe limitation, exacerbated by the restrictions imposed on the amplifier design to maintain sufficiently large cooling ranges, related to saturation of the ability of the crystal to absorb energy from the pumping laser. We further used the wave-optics modeling to include the amplification of the broadband pickup radiation including effects related to a finite bandwidth and host medium

dispersion.

The wave-optics modeling techniques presented in this thesis made a major impact on the design of the OSC test at Fermilab. Specifically, the elaborated simulation framework was used to show a single focusing lens, even without depth-of-field suppression, has essentially the same effective kick as the more cumbersome three-lens telescope designed for depth-of-field suppression. This in turn, due to a decrease in the transport lines total optical thickness, allowed for a decrease in the beam optics M_{56} enabling a switch to a test of the passive OSC at 950 nm light. With the transition to 950 nm light brings an increase in the OSC damping rates of approximately a factor of 5 and the ability to use cheaper and more sensitive detectors for diagnostics and alignment. We also presented a diagnostic technique for the longitudinal alignment of the pickup radiation and particle at the entrance of the kicker.

Additionally, although the OSC damping rates had already been known, here we examined them in further detail than had been done previously. The most significant result of this work was a deeper understanding of the dynamics of the particle in the damping process leading to an expansion of the so called cooling boundary. Finally horizontal rates were verified using the particle tracking code ELEGANT where we also examined the effects of particle and radiation separation and nonlinear path lengthening for a particle traveling from pickup to kicker center.

REFERENCES

[1] G. .I. Budker, Soviet Atomic Energy, **22** (5), 438 (1967).

[2] S. Nagaitsev, et al., Phys. Rev. Lett. **96**, 044801 (2006).

[3] V. N. Litvinenko, et al. in Proceedings of the International Workshop on Beam Cooling and Related Topics (COOL'17), Bonn, Germany, p. 77 (2017).

[4] A. A. Mikhailichenko, M.S. Zolotorev, Phys. Rev. Lett. **71**, 4146 (1993).

[5] M. S. Zolotorev, A. A. Zholents, Phys. Rev. E **50** 3087 (1994).

[6] V. A. Lebedev et al., in Proceedings of the North American Particle Accelerator Conference (NAPAC'13), Pasadena, CA, USA, p.422 (2013).

[7] M. Blaskiewicz, Annu. Rev. Nucl. Part. Sci. **64**, 299 (2014).

[8] M. Babzien, I. Ben-Zvi, I. Pavlishin, I. V. Pogorelsky, V. E. Yakimenko, A. A. Zholents, and M. S. Zolotorev, Phys. Rev. ST Accel. Beams **7**, 012801 (2004).

[9] A. Zholents and M. Zolotorev, W. Wan, Phys. Rev. ST Accel. Beams **4**, 031001 (2001).

[10] V. Lebedev, in proceedings of the 52nd Advanced Beam Dynamics Workshop on High-Intensity and High-Brightness Hadron Beams (HB2012), Beijing, China, September 17-21, 2012

[11] S. van der Meer. *Stochastic Damping of Betatron Oscillilations in the ISR.* Geneva, Switzerland (1972).

[12] D. Möhl, G. Petrucci, L. Thorndahl and S. van der Meer, Physics Reports **58** (2), pp. 73-119 (1980).

[13] P. Bramham, G. Carron, H.G. Hereward, K. Hubner, W. Schnell, L. Thorndahl, Nucl. Instrum. Meth. 125 , 201 (1975).

[14] D. Möhl, *Stochastic Cooling of Particle Beams*, Springer (2013).

[15] R. J. Pasquinelli., JINST **6** T08002 (2011).

[16] S. Antipov et al,. JINST **12**, T03002 (2017).

[17] V. Shiltsev. J. Phys.: Conf. Ser. **888** 012043 (2017).

[18] H. Weidemann, *Particle Accelerator Physics*. 3rd ed. Springer (2007).

[19] M. Conte, W.W. MacKay, *An Introduction to the Physics of Particle Accelerators*, 2nd ed. World Scientific (2008).

[20] A. A Zholents, Phys. Rev. Special Topcis-Accelerator and Beams **15** 032801 (2012).

[21] V. A. Lebedev, *Optical Stochastic Cooling*, ICFA Beam Dyn. Newslett. **65** pp. 100-116 (2014).

[22] H. H. Li, J. Phys. Chem. Ref. Data **9**, 161 (1980).

[23] O. Chubar, P. Elleaume, in the Proceedings of the European Particle Accelerator Conference (EPAC'98), Stocholm, Sweden, p.1177 (1998).

[24] O. Chubar et al., J. Phys. Conf. Ser. **425** (2013)

[25] O. Chubar, et al., in the Proceedings of the 2007 Free-Electron Laser conference (FEL07), p. 192 (2007).

[26] M.B. Andorf et al., Nucl. Instrum. Meth A **883** 119 (2018).

[27] P. E. Powers. *Fundamentals of Nonlinear Optics.* CRC Press. (2011).

[28] Landolt-Börnstein. *Numeric Data and Functional Relationships in Science and Technology-New Series*. vol. **41**, subvolume B. Springer (1999).

[29] I. T. Sorinka, K.L. Vodopyanov (Eds.) *Solid-State Mid-IR Laser Sources* Springer-Verlag (2003).

[30] G. Slack. Phys. Rev. B **6** (10) 3791 (1972).

[31] D.T.F Marple. J.Appl. Phys. **35**, 539 (1964).

[32] W. Kochner, *Solid-State Laser Engineering*, 5th ed. Springer (1999).

[33] J. E. Geusic et al., Appl. Phys. Lett. **4** (10). p. 182 (1964).

[34] P. Albers et al., J. Opt.Soc. Am. B **3** (1), p. 134 (1986).

[35] I. Moskalev et al., Optics. Exp. **24** (18) p.21090 (2016).

[36] S. B. Mirov et al., IEEE J. of Selected Topics in Quantum Electronics, **21**, (1) 1601719 (2014).

[37] A. A. Zholents, M. S. Zolotorev, in the Proceedings of Particle Accelerator Conference (PAC'97), Vancouver, B.C. Canada, p.1804 (1997).

[38] A. E. Siegman, *Lasers*, University Science Books (1986).

[39] M. B Andorf et al., in the Proceedings of the International Particle Accelerator Conference (IPAC'16), Busan, Korea, 3024 (2015).

[40] Titan CW Ti:Sapphire Laser Operation Manual. Q-Peak Inc.

[41] K. F. Wall et al., Opt. Lett. **14**(3), 180 (1989).

[42] M.B Andorf et al., in the Proceedings of the North American Particle Accelerator Conference (NAPAC'16), Chicago,IL, USA. p.3024 (2015).

[43] R. Palmer, Proceedings of the 1994 Advanced Accelerator Conference (AAC'94), AIP Conference Proceedings, 335, p.94 (1995).

[44] N. G. Gravilov et al., Nucl. Instrum. Meth A. **304** 63 (1991).

[45] M. Borland ELEGANT *: A flexible SDDS-Compliant Code for Accelerator Simulation*, Advanced Photon Source LS-287, September (2000).

[46] V. A. Lebedev and A.L. Romanov, in the Proceedings of International Workshop on Beam Cooling and Related Topics (COOL'15), Richmond VA, USA, p.123 (2015).

[47] S. Strogatz, *Nonlinear Dynamics and Chaos*, Perseus Books (1994).

[48] M. Boas, *Mathematical Methods in the Physical Sciences*, 3rd ed. John Wiley and Sons, (2006).

APPENDIX A

LONGITUDINAL EQUATIONS OF MOTION WITH OSC

In this appendix we derive the Equations of motion for a particle in the longitudinal phase space with an OSC insertion somewhere in the ring[1]. In general the timing between the wave packet radiation coming from the pickup and the arrival of the reference particle may be such that the reference particle is kicked. To account this we include an additional term phase ψ in describing the OSC kick. Traveling between pickup and kicker centers the particle is longitudinally displaced an amount $s = M_{56}u$

$$\Delta U_{osc} = \Delta\mathcal{E}\sin(k_o M_{56}\frac{u}{U_s} + \psi) \tag{A.1}$$

where $u = U - U_s$ is the difference in energy from the reference particle, $k_o \equiv 2\pi/\lambda_l$ and M_{56} is transfer matrix from pickup to kicker centers. The energy gained per turn is

$$\Delta U = qV sin(\phi) + \Delta U_{osc} \tag{A.2}$$

Then the change in u per turn is

$$\Delta u = qV\big(\sin(\phi) - \sin(\phi_s)\big) + \Delta\mathcal{E}\bigg(\sin(k_o M_{56}\frac{u}{U_s} + \psi) - \sin(\psi)\bigg) \tag{A.3}$$

The change in energy per turn is small so that the time derivative of u can be approximated by dividing by the revolution period $\tau_s = \frac{2\pi}{\omega_s}$

$$\frac{du}{dt} \approx \Delta u\frac{\omega_s}{2\pi}. \tag{A.4}$$

[1]The derivation of the longitudinal equations of motion (which do not include the OSC) developed in [19] were used as a guide.

Next we note that $\Delta\theta = \omega_{rf}\Delta\tau$ where $\Delta\tau$ is the change in the particles revolution period. This energy dependent change is characterized by the phase-slip factor which is determined by the rings lattice momentum compaction factor α_p and the beam energy:

$$\frac{d\tau}{\tau_s} = (\frac{1}{\gamma^2} - \alpha_p)\frac{\delta p}{P}. \tag{A.5}$$

Letting $\eta \equiv (1/\gamma^2 - \alpha_p)$ we find

$$\dot{\theta} \approx \frac{\Delta\theta}{\tau_s} = \frac{h\omega_s\eta}{U_s}u \tag{A.6}$$

where it was assumed the particle is relativistic so that $\delta p/P = u/U_s$. Eq's A.4 and A.6 describe a particles trajectory in the longitudinal phase space.

APPENDIX B

LARGE AMPLITUDE FIXED POINTS FROM OSC

In Chapter **??** we found a coupled set of nonlinear differential equations

$$\begin{aligned} \dot{a_x} &= -2J_0(a_s)J_1(a_x)\cos(\psi_{te})\lambda_x \\ \dot{a_s} &= -2J_0(a_x)J_1(a_s)\cos(\psi_{te})\lambda_s \end{aligned} \tag{B.1}$$

describing the damping of the particles betatron and synchrotron motion. a_x and a_s are the amplitudes of longitudinal displacement of the particle due to betatron and synchrotron motion respectively in the linear approximation of particle orbits, expressed in terms of the pickup radiation light wavelength and $J_n(x)$ is the nth Bessel function of the first kind. For the analysis we will at first assume $\psi_{te} = 0$ but later remove this restriction.

Fixed points correspond to a coordinate in the a_x, a_s phase space where both $\dot{a_x} = \dot{a_s} = 0$. It is straight forward to see that fixed points occur only when both $J_1(a_x) = J_1(a_s) = 0$ or $J_0(a_x) = J_0(a_s) = 0$.

Because we are interested in the behavior near fixed points, where nonlinearity is small, we can linearize the system by computing the Jacobian [47]

$$A = \begin{bmatrix} \frac{d\dot{a_x}}{da_x} & \frac{d\dot{a_x}}{da_s} \\ \frac{d\dot{a_s}}{da_x} & \frac{d\dot{a_s}}{da_s} \\ \end{bmatrix} = \begin{bmatrix} -J_0(a_s)\Big(J_0(a_s) - J_2(a_s)\Big)\lambda_x & 2J_1(a_x)J_1(a_s)\lambda_x \\ 2J_1(a_x)J_1(a_s)\lambda_s & -J_0(a_x)\Big(J_0(a_s) - J_2(a_s)\Big)\lambda_s \end{bmatrix} \tag{B.2}$$

so that

$$\begin{bmatrix} \dot{a_x} \\ \dot{a_s} \end{bmatrix} \approx A \begin{bmatrix} a_x \\ a_s \end{bmatrix} \tag{B.3}$$

and in the above equation A is evaluated once at some particular fixed point. Recall the most general solution of Eq. B.3 is $\boldsymbol{a}(t) = c_1\boldsymbol{v}_1\exp(\lambda_1 t) + c_2\boldsymbol{v}_2\exp(\lambda_2 t)$ where c_k is determined by the initial condition, λ_k and $\boldsymbol{v}_k$ are the eigenvalues are eigenvectors of A. Thus we can classify the fixed points as stable node if both eigenvalues are negative, an unstable node if

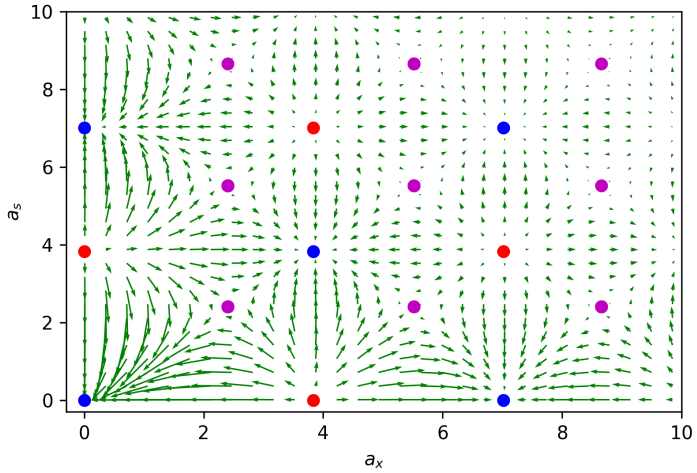

Figure B.1: The flow field of the Eq. B.2. Blue and red dots are the $J_1 = 0$ stable and unstable fixed points. The purple dots are saddle points corresponding to the $J_0 = 0$ fixed points.

both eigenvalues are positive and a saddle point if the eigenvalues have opposite signs. In this particular system the eigenvalues at fixed points are never complex and we thus have no spiral or closed orbit solutions.

Let us first consider the $J_1 = 0$ fixed points. There is a useful identity [48]

$$J_{n-1}(x) + J_{n+1}(x) = \frac{2n}{x} J_n(x) \tag{B.4}$$

which at the J_1 fixed points implies $J_0(\mu_{1,j}) = -J_2(\mu_{1,j})$ where j is zero or a positive integer. Thus A becomes

$$-2 \begin{bmatrix} J_0(a_s = \mu_{1,j}) J_0(a_x = \mu_{1,i}) \lambda_x & 0 \\ 0 & J_0(a_s = \mu_{1,j}) J_0(a_x = \mu_{1,i}) \lambda_s \end{bmatrix} \tag{B.5}$$

where i is also either zero or a positive integer. It is trivial to show the eigenvalues are $\lambda = -2J_0(\mu_{1,j})J_0(\mu_{1,i})\lambda_x$ and $\lambda = -2J_0(\mu_{1,j})J_0(\mu_{1,i})\lambda_s$. Clearly both eigenvalues have the

same sign and therefore these fixed points are nodes. For zero or even j $J_0(\mu_{1,j}) > 0$ and for odd j $J_0(\mu_{1,j}) < 0$ thus if $i + j$ is even (or zero) the node is stable and if $i + j$ is odd the node is unstable.

For the $J_0(\mu_{0,j}) = 0$ fixed points we immediately get

$$2 \begin{bmatrix} 0 & J_1(\mu_{0,j})J_1(\mu_{0,i})\lambda_x \\ J_1(\mu_{0,j})J_1(\mu_{0,i})\lambda_s & 0 \end{bmatrix} \tag{B.6}$$

and thus the eigenvalues are $\pm J_1(\mu_{0,j})J_1(\mu_{0,i})\sqrt{\lambda_x\lambda_s}$. The eigenvalues are always opposite in sign and so these fixed points are saddle points.

Now we may let ψ_{te} have an arbitrary value. We only need to consider the sign of $\cos(\psi_{te})$ when this is positive there is no qualitative difference in the phase portrait. When $\cos(\psi_{te}) < 0$ the saddle points will remain saddle points as the eigenvalues will still have different signs. The J_1 fixed points will switch polarity as their eigenvalues will change sign.

APPENDIX C

LAMBERT-W FUNCTION AS A TRANSCENDENTAL SOLUTION TO STEADY-STATE AMPLIFIER GAIN

In this appendix we show that when $\sigma_{pe} = 0$, Eq. 5.8 can be solved using the transcendental Lambert W function defined such that if $y = xe^x$ then $x = W(y)$ from which it follows that

$$x = W(xe^x). \tag{C.1}$$

$\sigma_{pe} = 0$ is actually the more common case in an amplifier. The equations we will develop here can be used with for example a Ti:sapphire amplifier or even a Cr:ZnSe amplifier pumped by an Erbium fiber laser which lases outside Cr:ZnSe's emission band.

Letting $\alpha = N_t\sigma_{pa}$ Eq. 5.8 becomes

$$\frac{dI_p}{dz} = \frac{-\alpha I_p}{I_p/I_{sat} + 1} \tag{C.2}$$

where $I_{sat} \equiv h\nu_p/\sigma_{pa}\tau_2$ is the saturation intensity, defined as such since it is clear that in the above equation that for $I_P << I_{sat}$ the pump attenuation is just the ordinary exponential decay. Eq. C.2 can be solved with the standard method of separation of variables

$$-z\alpha_o = ln\left(\frac{I_p}{I_{po}}\right) + \frac{I_p - I_{po}}{I_{sat}} \tag{C.3}$$

yielding a transcendental equation. Rearranging the above equation gives

$$\frac{I_p}{I_{sat}}\exp(I_p/I_{sat}) = \frac{I_{po}}{I_{sat}}\exp(-\alpha z + I_{po}/I_{sat}) \tag{C.4}$$

and identifying $x = I_p/I_{sat}$ in Eq. C.1 we evidently have

$$I_p(z) = I_{sat}W\left(\frac{I_{po}}{I_{sat}}\exp(-\alpha z + I_{po}/I_{sat})\right). \tag{C.5}$$

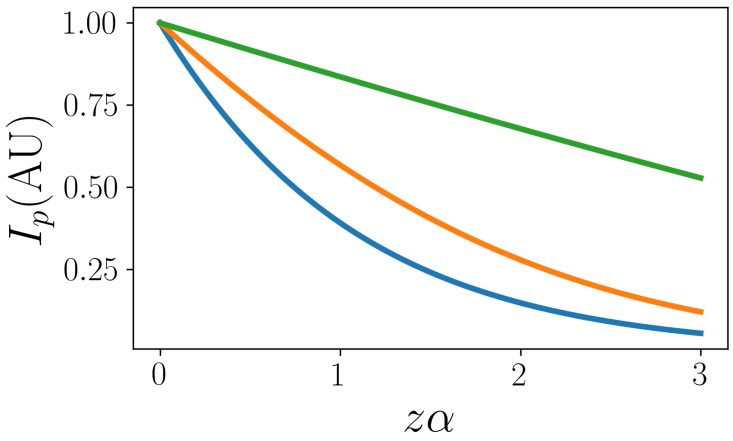

Figure C.1: Absorption of a pump laser through a gain medium for three different incident pump intensities: $I_{po} = 0.1I_{sat}$ (blue), $I_{po} = I_{sat}$ (orange) and $I_{po} = 5I_{sat}$ (green).

Then referring to Eq. 5.6 the small signal gain of a plane-wave is finally given by

$$G = \exp\left[\frac{\sigma_s \tau_2}{h\nu_p}\left(I_{po} - I_{sat} W\left(\frac{I_{po}}{I_{sat}}\exp(-\alpha z + I_{po}/I_{sat})\right)\right)\right] \tag{C.6}$$

In Fig. C.1 the pump intensity passing through a gain medium is plotted for three different values of I_{sat}. When $I_{po} = 0.1I_{sat}$ the absorption is essentially exponential. At larger intensities the population of the ground state becomes depleted and there is a corresponding increase in the pump transmission. The W function is built into SciPy's library of special functions and was used to make the plots.